# Transport-driven Scrape-Off-Layer flows and the boundary conditions imposed at the magnetic separatrix in a tokamak plasma



INSTITUTE OF PHYSICS PUBLISHING and INTERNATIONAL ATOMIC ENERGY AGENCY NUCLEAR FUSION

Nucl. Fusion **44** (2004) 1047–1066 PII: S0029-5515(04)82014-3

# Transport-driven Scrape-Off-Layer flows and the boundary conditions imposed at the magnetic separatrix in a tokamak plasma

**B. LaBombard, J.E. Rice, A.E. Hubbard, J.W. Hughes, M. Greenwald, J. Irby, Y. Lin, B. Lipschultz, E.S. Marmar, C.S. Pitcher[a], N. Smick, S.M. Wolfe, S.J. Wukitch and the Alcator Group**

Massachusetts Institute of Technology, Plasma Science and Fusion Center, 175 Albany St., Cambridge, MA 02139, USA

E-mail: labombard@psfc.mit.edu.

Received 4 May 2004, accepted for publication 4 August 2004
Published 9 September 2004
Online at stacks.iop.org/NF/44/1047
doi:10.1088/0029-5515/44/10/001

**Abstract**

Plasma profiles and flows in the low- and high-field side scrape-off-layer (SOL) regions in Alcator C-Mod are found to be remarkably sensitive to magnetic separatrix topologies (upper-, lower- and double-null) and to impose topology-dependent flow boundary conditions on the confined plasma. Near-sonic plasma flows along magnetic field lines are observed in the high-field SOL, with magnitude and direction clearly dependent on X-point location. The principal drive mechanism for the flows is a strong ballooning-like poloidal transport asymmetry: parallel flows arise so as to re-symmetrize the resulting poloidal pressure variation in the SOL. Secondary flows involving a combination of toroidal rotation and Pfirsch–Schlüter ion currents are also evident. As a result of the transport-driven parallel flows, the SOL exhibits a net co-current (counter-current) volume-averaged toroidal momentum when $B \times \nabla B$ is towards (away from) the X-point. Depending on the discharge conditions, flow momentum can couple across the separatrix and affect the toroidal rotation of the confined plasma. This mechanism accounts for a positive (negative) increment in central plasma co-rotation seen in L-mode discharges when $B \times \nabla B$ is towards (away from) the X-point. Experiments in ion-cyclotron range-of-frequency-heated discharges suggest that topology-dependent flow boundary conditions may also play a role in the sensitivity of the L–H power threshold to X-point location: in a set of otherwise similar discharges, the L–H transition is seen to be coincident with central rotation achieving roughly the same value, *independent* of magnetic topology. For discharges with $B \times \nabla B$ pointing away from the X-point (i.e. with the SOL flow boundary condition *impeding* co-current rotation), the same characteristic rotation can only be achieved with *higher* input power.

**PACS numbers:** 52.30.-q, 52.25.Fi, 52.25.Gj, 52.40.Hf, 52.55.Fa, 52.70.Ds, 52.70.Nc

## 1. Introduction

Plasma flow along magnetic field lines has been measured in the scrape-off-layer (SOL) of many tokamaks [1–12], with velocities approaching a significant fraction of the local sound speed. While such strong flows are expected on field lines close to a material surface, these flows are found in regions far from any surface. The physical mechanism(s) behind such flows is an active area of research, since depending on the drive mechanisms and resultant total velocity vectors, these flows may affect the impurity compression of the divertor, the transport of impurities in the SOL plasma and perhaps the balance of material erosion and re-deposition between the inner and outer divertor legs, all of which can impact future reactor devices such as ITER [13].

A number of mechanisms are known to yield parallel flows in the SOL: ionization imbalances, Pfirsch–Schlüter

[a] Presently at 132 Bowood Ave., Toronto M4N1Y5, Canada.

flows, poloidal transport asymmetries (e.g. ballooning-like transport), and toroidal rotation. Analytic models and numerical simulations [8, 9, 14–18] have investigated such effects with the goal of reproducing observed flows and assessing their impact on impurity distributions. While in some cases models have produced flows similar to those measured (e.g. JT-60U [19]), there are other cases where the measured flows appear too large (e.g. JET [9]). One difficulty is the complexity of the flow pattern. Parallel flows measured near material surfaces (e.g. in the divertor) are largely independent of those far away [10], which in turn may have spatial variation. In this regard, multipoint flow measurements far from the divertor are desired but rarely available.

Despite large differences in first-wall and divertor geometries among experimental devices, parallel flows measured at locations far from material surfaces exhibit remarkably similar characteristics. In diverted discharges, there is a tendency for the plasma to flow along field lines in the co-current direction near the separatrix. This is seen at locations 'upstream' of the outer divertor (JT-60U [8], C-Mod [7]), near the outer midplane (TCV [12], C-Mod [7]) and near the top of the poloidal cross-section (JET [9]). These flows tend to reverse (although sometimes not symmetrically) when the magnetic field is reversed. In JT-60U, only slight perturbations to the parallel flows ($< \sim$20%) were seen during conditions of strong gas-injection and divertor pumping [20]—evidence that these flows are dominated by effects other than ionization and fuelling imbalances.

In retrospect, measurements of SOL flows in limiter discharges (Alcator C [1], T-10 [2], DITE [4]) also exhibited many features seen in diverted discharges. The drive mechanisms for these were associated with a combination of ballooning-like cross-field transport asymmetries [21] and co-current toroidal rotation. Co-current rotation is a natural consequence of the positive radial electric field that exists on open field lines in the SOL [22]; it is a divergence-free $E \times B$ motion ($V_\phi = E_r/B_\theta$, $V_\theta = 0$), incurring minimal resistance in the axisymmetric geometry. Results from divertor biasing experiments in TdeV clearly demonstrated this effect [6]: in response to an applied radial electric field, the SOL plasma simply rotated toroidally. Ballooning-like cross-field transport is a more intractable mechanism; since there is no theoretical prescription for the magnitude and poloidal distribution of plasma turbulence and associated cross-field transport, it remains a free parameter in models. In fact, in circumstances where parallel flows are dominated by ballooning-like transport asymmetries, a direct measurement of such *transport-driven flows* can reveal key missing information about the underlying plasma turbulence and transport.

Another potentially important aspect of the SOL flows, which has been largely overlooked, is the effect that they might have on the core plasma. Do these experimentally observed SOL flows influence the boundary conditions on the confined plasma in any significant way? Measurements of central plasma toroidal rotation in Alcator C-Mod have uncovered clear connections between the rotation profile and the operation of the tokamak in a variety of energy confinement modes [23]. It is important to note that these observations were made in ion-cyclotron range-of-frequency (ICRF) heated discharges, with no external source of momentum input—a situation that is expected in a reactor-scale device such as ITER. Immediately after an L–H transition, a prompt increase in co-current rotation is seen, starting near the edge and propagating into the plasma centre over timescales of the order of the energy confinement time [24]—clear evidence that flow conditions near the edge influence central plasma rotation. Interestingly, the central rotation speed in the Ohmic L-mode was found to depend on the magnetic topology, favouring stronger counter-current rotation in upper versus lower X-point discharges with otherwise similar conditions ($B \times \nabla B$ directed downward) [23]. Since these plasmas had no external toroidal momentum input, the key difference must be associated with the boundary conditions imposed on the confined plasma, e.g. the toroidal projection of the plasma flows near the separatrix in the SOL.

This paper addresses both aspects of plasma flows on Alcator C-Mod from an experimental point of view: (1) the observed SOL flow pattern and principal drive mechanisms responsible and (2) the resultant toroidal flow boundary conditions seen by the confined plasma at the separatrix. Our investigation is based on new plasma profile and flow information from scanning probes located in both the high- and low-field SOL regions as well as core plasma rotation measurements. The research has revealed a rich interplay among anomalous cross-field transport, strong plasma flow along magnetic field lines, magnetic topology and toroidal rotation in the edge plasma. In particular, remarkably rapid plasma flows parallel to magnetic field lines are observed in the high-field SOL. Their origins are traced to a strong ballooning-like component of the cross-field transport, which is particularly manifest in a comparison of high- and low-field side SOL profiles in near double-null discharges. We have also found that the SOL plasma flows do indeed impose influential boundary conditions on the confined plasma, setting the toroidal rotation of the plasma near the separatrix and, as a result, affecting the toroidal rotation of the plasma as a whole. Moreover, our research suggests that topology-dependent SOL flow boundary conditions may offer an explanation for the dependence of the L–H power threshold on the X-point location: in a set of otherwise similar discharges, the L–H transition is observed to coincide with co-current plasma rotation achieving roughly the same value in both upper- and lower-null topologies (with $B \times \nabla B$ down). However, in upper-null, the SOL flow boundary condition *impedes* co-current plasma rotation. Correspondingly, a higher input power (which in itself tends to spin the plasma in the co-current direction through an increase in stored plasma energy [25]) is seen necessary for attaining the H-mode in this topology.

Section 2 briefly outlines the key plasma flow diagnostics for this study: a magnetically driven fast-scanning swing-probe near the midplane on the high-field SOL [26], two scanning-Mach probes on the low-field SOL [11] and core plasma rotation inferred from the Doppler shifts of central $Ar^{17+}$ ions [23]. Section 3 reports results from a set of experiments aimed at sorting out the principal drive mechanisms responsible for the observed SOL flows. These data reveal three flow components: a strong flow along magnetic field lines from the low- to high-field SOL, toroidal plasma rotation and Pfirsch–Schlüter flow. In addition, data from different magnetic topologies (lower X-point,

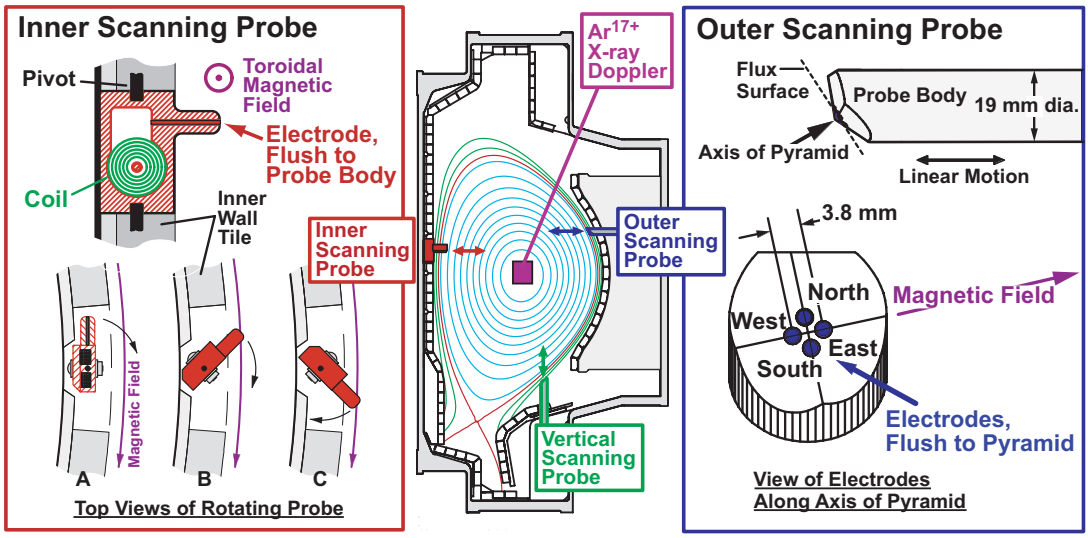


**Figure 1.** Scanning Langmuir–Mach probes are used to infer simultaneously plasma profiles and parallel flows at three locations in the SOL of Alcator C-Mod, including the high-field side (inner scanning probe). In addition, core plasma rotation is inferred from the Doppler shifts of central $Ar^{17+}$ ions. A typical lower single-null (LSN) plasma equilibrium is shown.

upper X-point, double-null) indicate that a ballooning-like component of the cross-field plasma transport is the underlying cause for the strong parallel flow—in single-null topologies, plasma exists on the high-field side SOL *principally because it flows along field lines from the low-field side*.

A simple flux-tube model of plasma flows is presented in section 4. Data from upper- and lower-null discharges (with $B \times \nabla B$ down) are combined to extract just the transport-driven, parallel component of the plasma flow. An estimate of the net particle source profile along flux tubes is constructed, elucidating the ballooning-like asymmetry of the cross-field particle transport and yielding rough estimates for effective particle transport velocity ($V_{\rm eff}$) and diffusion ($D_{\rm eff}$) coefficients. This data-constrained model also clearly illustrates how the SOL can possess a net volume-averaged co-current (counter-current) toroidal momentum when the $B \times \nabla B$ direction is towards (away from) the X-point.

Section 5 examines connections between plasma flows near the separatrix and in the plasma centre. A clear correspondence is noted, demonstrating that the topology-dependent SOL flows set flow boundary conditions for the confined plasma and affect the radial electric fields near the separatrix. Finally, a set of experimental observations is presented in section 6 that suggest the magnetic topology, SOL flows, toroidal rotation and dependence of the L–H power threshold on the X-point location are fundamentally connected. Concluding remarks are contained in section 7.

## 2. Experiment and flow diagnostics

Background information on Alcator C-Mod's design, diagnostics and operational characteristics can be found in [27]. A cross-section of a typical Alcator C-Mod equilibrium used for the present study and locations of key plasma flow diagnostics are shown in figure 1. The results reported in this paper were obtained from a variety of Ohmic heated deuterium discharges, including plasma currents ($I_{\rm p}$) between 0.5 and 1.0 MA, toroidal magnetic field strength ($B_{\rm T}$) between 4 and 6 T and line-averaged plasma densities, $0.8 < \bar{n}_{\rm e} < 2.4 \times 10^{20}\,{\rm m}^{-3}$ plus some ICRF heated discharges (discussed further in section 6) that exhibited an L–H transition. The influence of magnetic topology (i.e. upper-, lower- and double-null) on plasma conditions was studied by fixing the direction of toroidal magnetic field and plasma current in the 'normal' direction ($B_{\rm T}$ and $I_{\rm p}$ aligned, $B \times \nabla B$ pointing down) and changing the magnetic flux balance between the upper and lower X-points. The effect of reversing the directions of $B_{\rm T}$ and $I_{\rm p}$ was studied for a subset of discharges (section 3.3). In this case, the magnetic topology was fixed in lower single-null, similar to that shown in figure 1.

Views of the outer scanning probe, located 11 cm above the midplane on the large major radius side of the torus, are shown in figure 1. The EAST and WEST tungsten electrodes, which are embedded in an electrically floating molybdenum body, sample plasma from opposite directions along the same field line, forming a 'Mach probe pair' in which the parallel Mach number can be estimated from the ratio of ion saturation current densities, $M_{\parallel} = 0.43 \ln(J_{\rm east}/J_{\rm west})$ [28]. By fitting positive- and negative-going $I$–$V$ characteristics from the EAST and WEST electrodes, electron densities ($n$), temperatures ($T_{\rm e}$) and parallel Mach numbers ($M_{\parallel}$) along the probe's trajectory are obtained every 0.25 ms (corresponding to ~0.25 mm of probe travel). The NORTH and SOUTH tungsten electrodes were operated in a floating-voltage mode (1 MHz sample frequency). These electrodes are used to estimate the poloidal phase velocity of plasma fluctuations. The vertical scanning probe (location shown in figure 1) is of similar construction [29] and is operated in the same manner.

The inner scanning probe, which is located 5.8 cm above the midplane on the small major radius side of the torus (figure 1), consists of a single tungsten electrode embedded in an electrically isolated carbon fibre composite graphite body and aligned flush with the surface of a short cylindrical arm that extends from the body. Its novel electromechanical actuation is based on the divertor bypass flaps designed by Pitcher [30]. In response to a voltage waveform applied to an embedded coil,

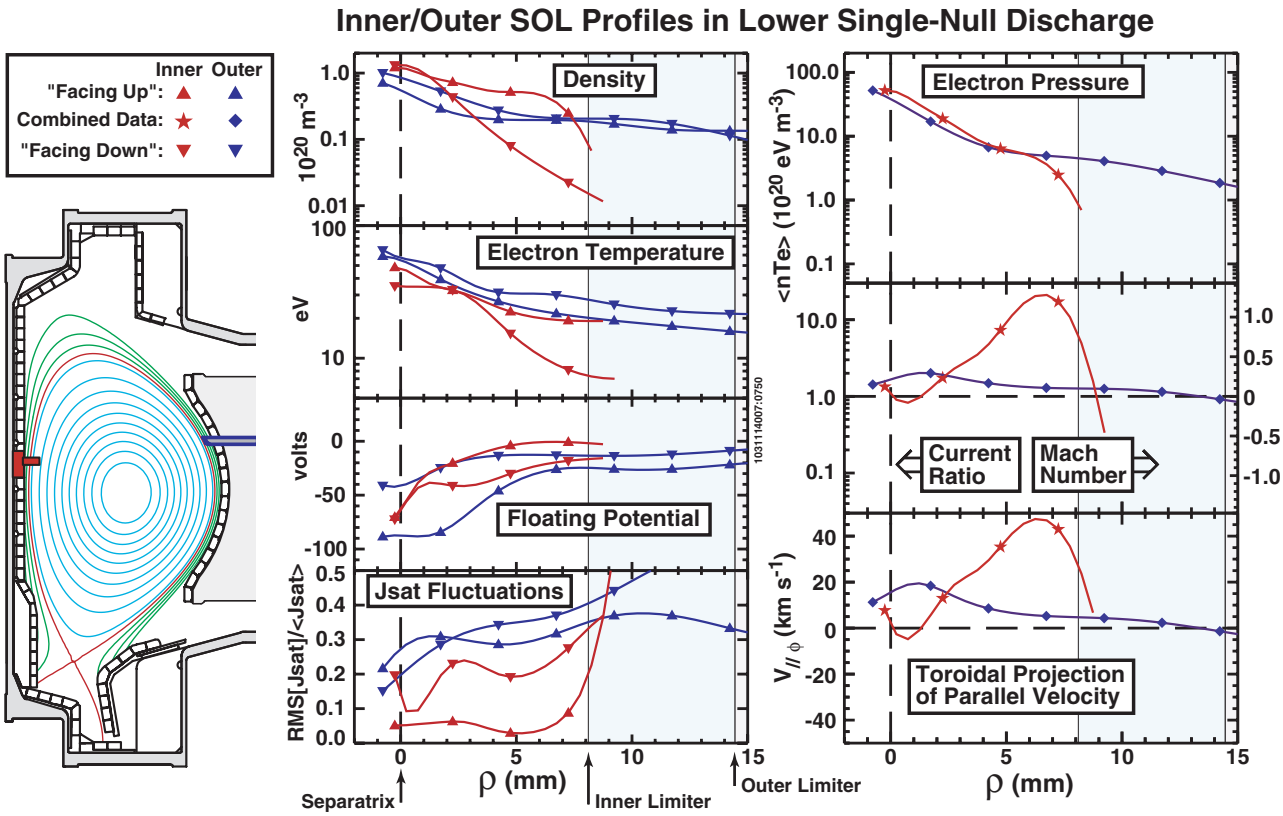


**Figure 2.** Magnetic equilibrium for lower single-null discharge and corresponding profile data recorded in the inner and outer regions of the SOL.

the probe body swings into the high-field side SOL, completing a 180° spin about its pivot axis. For angles less than 90°, the flush-mounted electrode samples plasma in one direction along a field line while for angles greater than 90° it samples the other. The single electrode is biased with respect to the graphite body with a swept-voltage waveform. In a manner similar to that for the other scanning probes, cross-field profiles of density, temperature and parallel Mach number are assembled. However, in this case the Mach number is computed from the ratio of the ion saturation current densities when the probe is looking 'upstream' versus 'downstream' along magnetic field lines. Owing to geometrical inaccuracies and concerns about interpreting probe data when field lines are nearly tangent to the electrode surface [31], data collected for pivot angles between ∼80° and ∼100° are excluded from the analysis.

The three probes are typically operated together, simultaneously executing two or three scans during a single discharge. The resultant data are mapped onto magnetic flux surfaces re-constructed from magnetic measurements [32] and the EFIT plasma equilibrium code [33]. The flux-surface coordinate used here, $\rho$, is defined as the distance into the SOL along a major radius at the outer midplane. Small shifts in the $\rho$-axis (up to 2 mm) have been applied to some probe data, using the SOL power balance as a constraint.

X-ray spectra along a toroidal line of sight tangent to the plasma centre ($R = 0.685$ m) are recorded using a fixed von Hamos type crystal x-ray spectrometer [23]. Central toroidal rotation velocities of $Ar^{17+}$ ions are inferred from the Doppler shifts of the corresponding $Ly_\alpha$ doublet. Trace amounts of argon are injected early in the discharge to facilitate the measurement. This technique avoids the use of neutral beams, which can add toroidal momentum to the plasma and perturb intrinsic self-generated flows. Owing to the high charge state of the argon ions, their toroidal rotation is expected to be well coupled and close to the toroidal rotation of the plasma background. This hypothesis is supported by an independent inference of toroidal plasma rotation through sawtooth oscillations [34, 35].

## 3. SOL profiles and flows

The scanning probes have yielded a wealth of information on cross-field plasma profiles, including plasma flow and their sensitivities to magnetic topology and discharge conditions. First, we compare inner and outer data from a set of three representative plasmas where only the X-point topology was changed: lower-single null (LSN), upper-single null (USN) and near-double null (DN). We then examine the effect of changing plasma density (section 3.2), followed by a compilation of information on poloidal plasma flows (section 3.3).

### *3.1. Effect of magnetic topology*

The magnetic equilibria and probe-inferred plasma profile data for representative LSN, USN and DN discharges are shown in figures 2–4. These were Ohmic L-mode plasmas ($I_p = 0.78$ MA, $B_T = 5.4$ T, $\bar{n}_e = 1.4 \times 10^{20}$ m$^{-3}$) with $B_T$ and $I_p$ aligned and $B \times \nabla B$ pointing down. The colour-coded profiles (red—inner SOL, blue—outer) are smooth spline curves, fitted

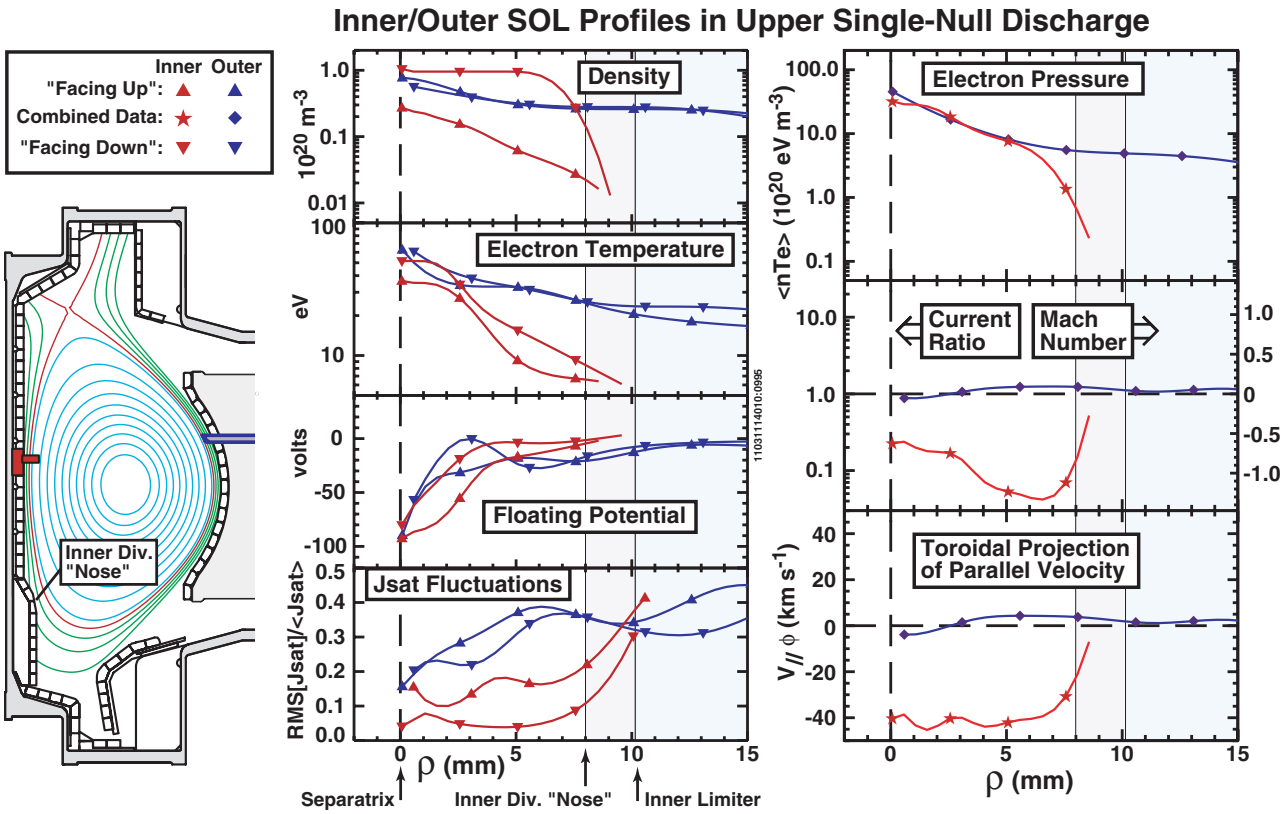


**Figure 3.** Same as figure 2 for upper single-null discharge.

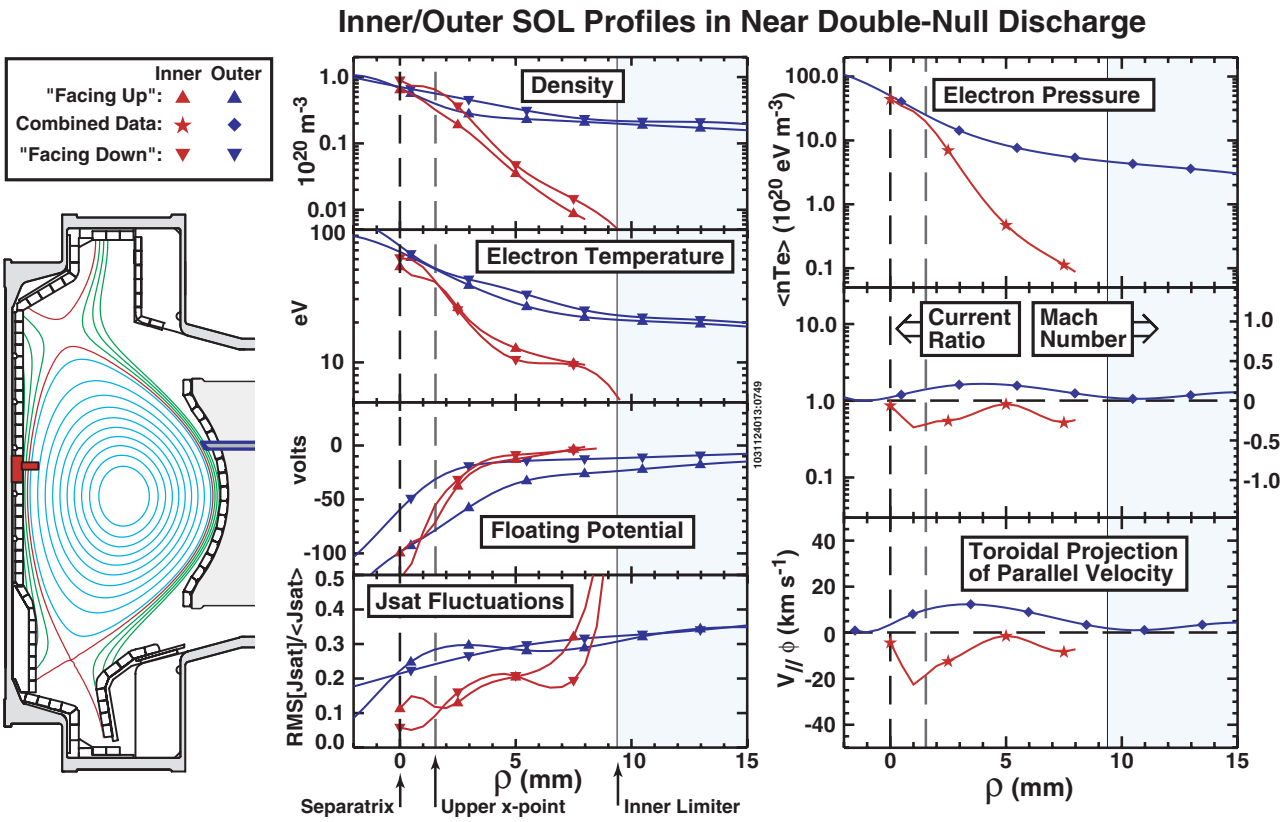


**Figure 4.** Same as figure 2 for near double-null discharge.

to data points recorded over the probes' trajectories. Typical $\rho$-spacings between individual data points were under 0.5 mm. The location of the magnetic separatrix ($\rho = 0$) is indicated, as well as locations that map to limiter surfaces. The data panels on the left show separate profiles recorded by 'facing up' and 'facing down' probes. A facing up (facing down) probe collects plasma from field lines immediately connected to regions vertically above (below) the probe in the cross-sectional views of figures 2–4. Thus, the EAST electrode on the outer probe continuously records data facing up, while the WEST records facing down. The inner probe collects data from the facing up direction when its pivot angle is less than 90°; otherwise it collects data from the facing down direction.

A description of the quantities plotted in figures 2–4 follows:

*Density, electron temperature, floating potential*—these are standard quantities from magnetized probe theory [36], derived separately for the facing up and facing down electrodes. No correction is applied to account for background plasma flow; the densities reported here are those that would be expected in the ambient plasma with no flow present. The variation of the inner probe's projected area during its motion is taken into account. However, it should be noted that owing to a non-ideal geometry and large clearances between electrode and probe body, the accuracy of the area estimate is uncertain (perhaps a ±50% error). Therefore, factors of ∼2 differences in density (or electron pressure) between inner and outer profiles are possibly within systematic errors.

$J_{\rm sat}$ *fluctuations*—the quantity shown is the rms ion saturation current fluctuation about the mean divided by the mean value. It is computed during the time interval when the probe's $I$–$V$ characteristic is in the ion saturation regime, an approximately 200 $\mu$s time window. Thus, it is a measure of relative turbulence amplitude, derived from the fluctuation power spectrum above ∼5 kHz.

*Electron pressure*—the average of $nT_{\rm e}$ for the facing down and facing up electrodes. This is a good first estimate of the ambient electron pressure, regardless of the background plasma flow speed.

*Current ratio*—is the ratio of local ion saturation current densities looking upstream and downstream along field lines. A ratio greater than 1 corresponds to flow in the co-current direction.

*Mach number*—this is computed using the Hutchinson formulation [28]. The formulation assumes the ratio of particle to momentum diffusivities to be unity; varying this ratio by a factor of 2 can lead to a 20% variation in the inferred $M_\parallel$. In addition, the theory is based on a uniform electron temperature; yet, significant electron temperature differences are evident on the facing up versus facing down electrodes (inner probe), which may introduce further errors. Positive $M_\parallel$ correspond to flow in the co-current direction.

*Toroidal projection of parallel velocity*— this is the quantity $V_{\parallel\phi} = M_\parallel C_{\rm s} B_\phi / B$, where $C_{\rm s}$ is the local sound speed (assuming $T_{\rm i} = T_{\rm e}$) and $B_\phi / B$ is the local ratio of toroidal to total magnetic field strength. Positive values of $V_{\parallel\phi}$ correspond to flow in the co-current direction.

Focusing on figures 2 and 3, a number of important observations can be made:

(1) In both topologies, the electron pressure roughly maps along field lines that connect between the inner and outer SOL. However, up/down averaged $T_{\rm e}$ are systematically lower in the inner SOL, indicating a higher up/down averaged value of $n$. This is particularly evident at locations far from the separatrix, $\rho \sim 5$ mm.

(2) The inner probe detects different $T_{\rm e}$ values (by as much as a factor of ∼2), depending on whether it is facing up or facing down. Comparing the LSN and USN data, one can see that the lower $T_{\rm e}$ values are recorded when the probe faces towards the inner divertor strike-point, independent of topology.

(3) Normalized $J_{\rm sat}$ fluctuation levels are a factor of 3–10 lower in the inner SOL compared with the outer—and this is on field lines that connect the two. Note that much of the up/down variation in this quantity on the inner SOL can be explained by the up/down variation in the mean current collected by the probe. However, inner/outer differences in normalized $J_{\rm sat}$ fluctuation levels cannot be explained by the variation in the means; factors of ∼3 differences in absolute $J_{\rm sat}$ fluctuation levels are implied.

(4) Large current asymmetries (>10 for LSN, <0.1 for USN) and parallel Mach numbers ($|M_\parallel| \sim 1$) are seen in the inner SOL. The measurements imply a co-current $V_{\parallel\phi}$ in LSN and counter-current $V_{\parallel\phi}$ in USN that has near-sonic speed near $\rho \sim 7$ mm. Near the separatrix, $V_{\parallel\phi}$ does not symmetrically reverse in going from LSN to USN; the data appear to reflect a counter-current offset of $M_\parallel \sim -0.3$.

(5) The magnitudes of $M_\parallel$ and $V_{\parallel\phi}$ in the outer SOL are much smaller, changing from co-current values of $M_\parallel < \sim 0.3$ in LSN to near zero or slightly negative values near the separatrix in USN.

Observations (1) and (2) are strong evidence for a poloidally asymmetric transport mechanism (ballooning-like) that preferentially exhausts plasma energy into the low-field (outer) SOL region. Apparently, $T_{\rm e}$ gradients arise so as to transport some of this power to the inner SOL region. The poloidal asymmetry in turbulence level inferred from (3) supports this picture. Similar asymmetries observed in inner/outer $D_\alpha$ fluctuation levels corroborate these measurements [37]. Observation (4) implies that the particle exhaust is also poloidally asymmetric. The strong parallel plasma flows on the inner SOL and their topology dependence may be simply interpreted as the plasma 'filling in' the inner SOL by parallel flow; excess particles that spill into the outer SOL stream along field lines into the inner SOL. Flow features in (4) and (5) that do not symmetrically reverse in going from LSN to USN may involve a combination of toroidal rotation and/or Pfirsch–Schlüter currents. (Differences in the upper/lower divertor geometry or inaccuracies in the facing up versus facing down probe areas could also play a role.)

Results from a DN discharge are shown in figure 4. Except for the magnetic topology, this discharge was a match in all respects to the LSN and USN discharges. Important observations are:

(6) The inner $T_{\rm e}$ and $n$ profiles are dramatically sharpened in DN discharges; the resultant electron pressure e-folding lengths exhibit a factor of ∼4 in/out asymmetry.

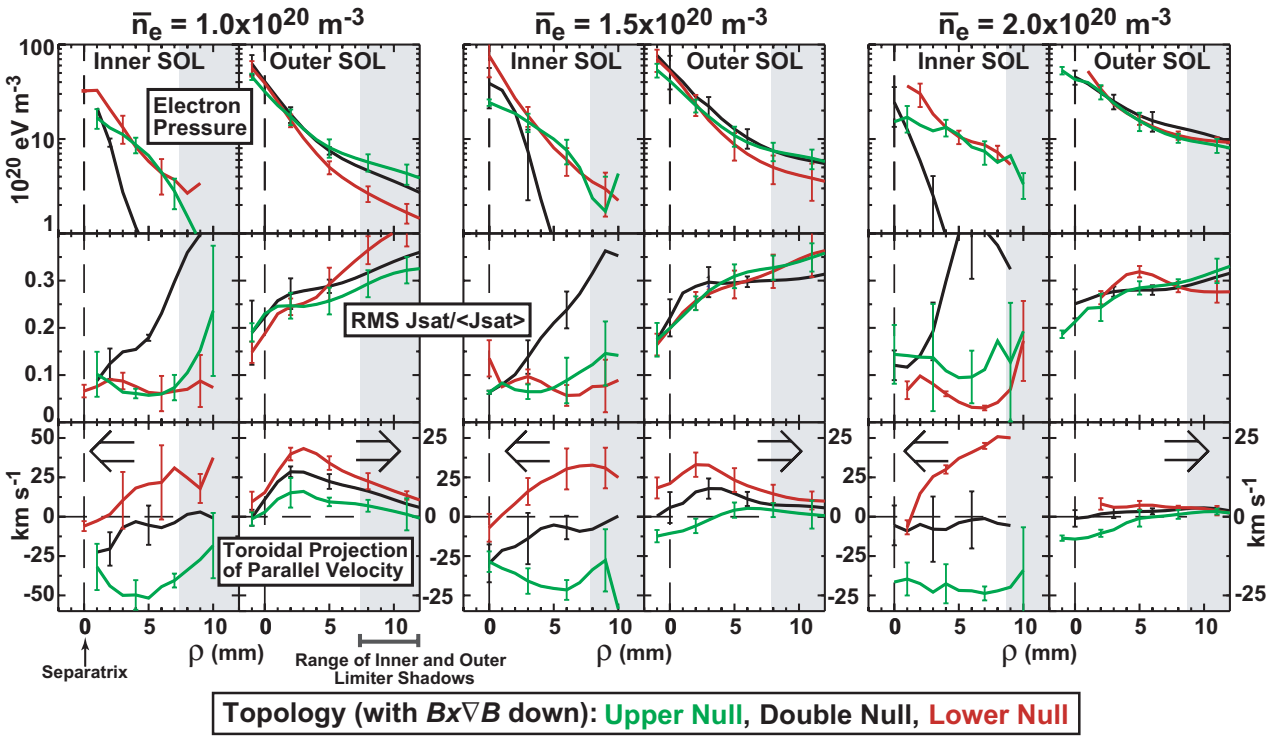


**Figure 5.** A compilation of inner and outer SOL profiles from 112 probe scans. Line-averaged density and magnetic topology were varied with otherwise identical conditions.

(7) In contrast to LSN and USN discharges, the inner probe detects no difference in $T_e$ values when it is facing up versus facing down.

(8) Normalized $J_{sat}$ fluctuation levels remain a factor of ~2 lower on the inner SOL. Accounting for the reduction in the mean ion saturation current level, the absolute $J_{sat}$ fluctuations are an order of magnitude or more lower in the inner versus outer SOL.

(9) The magnitude of $V_{\|\phi}$ on the inner SOL is greatly reduced compared with LSN and USN.

(10) The outer $V_{\|\phi}$ profile does not go to zero. It exhibits values that are intermediate between LSN and USN.

The most compelling evidence for the existence of a strong ballooning-like transport mechanism is (6), which is augmented by (8). Further supporting evidence comes from recent $D_\alpha$ camera measurements [38]: for discharges in which the magnetic flux balance is swept in time from LSN to USN, the region of sharp e-folding length in the high-field SOL is seen to track with the secondary separatrix. Observation (7) is somewhat expected. But, most importantly, it tells us that the up/down $T_e$ differences seen in LSN and USN discharges (2) should be taken seriously. In light of all the other observations, (9) is now completely expected; without a connection between the inner and outer SOL along field lines, the mechanism that drives strong parallel flow is absent. The residual parallel flow (10) near the outer midplane in this up/down symmetric topology is interesting and suggestive of toroidal rotation and/or Pfirsch–Schlüter ion flow effects.

### *3.2. Effect of plasma density*

Profiles and flows from a large set of discharges were collected to gain better statistics and to examine the effect of changing line-averaged density. A compilation of electron pressures (up/down averaged), normalized $J_{sat}$ fluctuations and $V_{\|\phi}$ profiles from 112 simultaneous probe scans in 44 discharges is shown in figure 5. The discharge conditions were: $I_p = 0.78$ MA, $B_T = 5.4$ T, $\bar{n}_e$ ranging from 0.88 to $2.2 \times 10^{20}$ m$^{-3}$ in LSN, USN and DN topologies (magnetic equilibria identical to those in figures 2–4). The data are binned into three line-averaged density categories, $\bar{n}_e = 1.0, 1.5, 2.0 \times 10^{20}$ m$^{-3}$ and colour-coded according to magnetic topology. Vertical bars indicate $\pm 1$ standard deviation, computed from the sample variance.

Figure 5 demonstrates that features seen in the individual discharges of figures 2–3 are robustly reproducible and persistent over the full range of densities: sharp in/out pressure gradient asymmetries in DN, lower fluctuation levels on inner SOL, strong (near-sonic) parallel plasma flow on inner SOL, with direction clearly dependent on magnetic topology. The combined data set also yields a lower electron pressure on the inner SOL relative to outer, with separatrix values being the lowest in USN. The inner and outer electron pressure profiles clearly flatten with increasing density—a trend that has been well documented for outer SOL data [39]. Concurrently, we see the magnitude of $V_{\|\phi}$ in the outer SOL decreasing with increasing $\bar{n}_e$. If we examine the profiles at the vertical probe location for the same set of discharges (figure 6), we see a similar trend of flattened pressure profiles and reduced magnitude of $V_{\|\phi}$ with increasing $\bar{n}_e$, although the $V_{\|\phi}$ profile tends to peak near the separatrix at low densities.

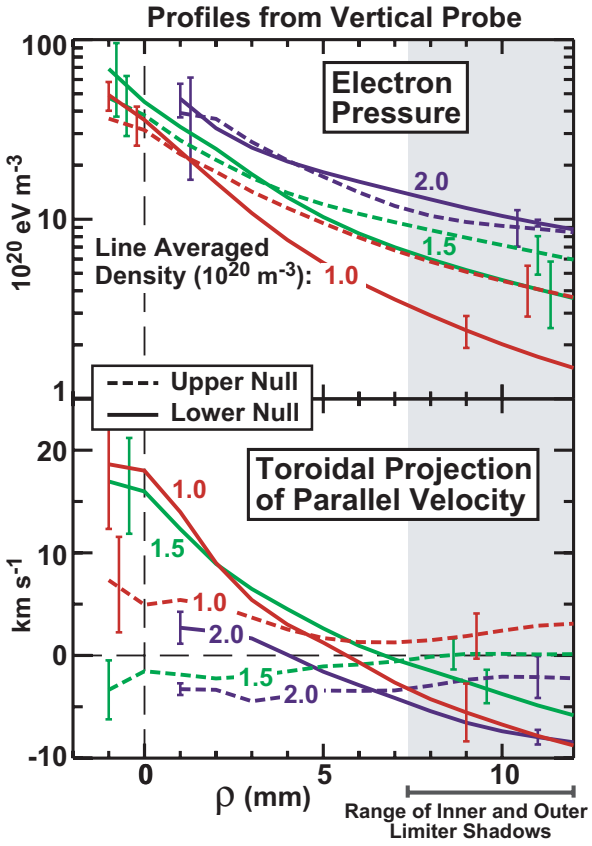


**Figure 6.** Profiles at the vertical probe location corresponding to the data shown in figure 5.

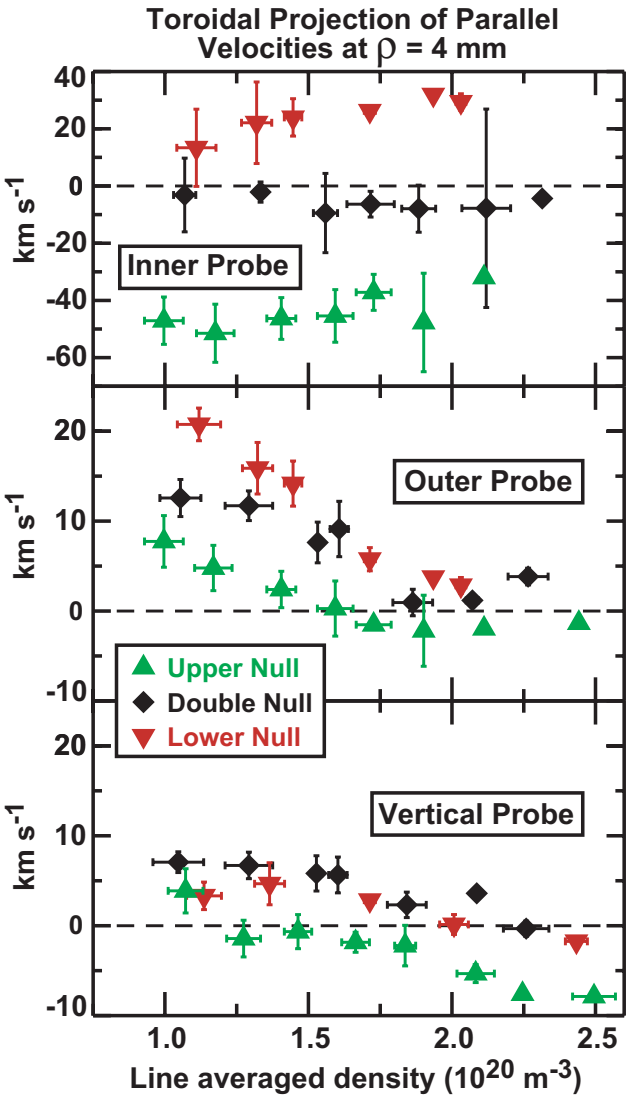


**Figure 7.** Toroidal projection of parallel flows versus $\bar{n}_e$ for the data set of figure 5. Data are binned in $\bar{n}_e$ increments. Bars indicate $\pm 1$ standard deviation, computed from sample variance.

In order to examine the density dependence in more detail, $V_{\parallel\phi}$ at $\rho = 4$ mm measured by the three probes are plotted versus $\bar{n}_e$ in figure 7. The flows in the inner SOL clearly behave differently from that in the outer SOL: the magnitude and direction of inner $V_{\parallel\phi}$ is insensitive to $\bar{n}_e$ and appears to be affected by topology alone. In contrast, the direction of $V_{\parallel\phi}$ at the outer probe location is persistently co-current at low densities. Its magnitude is affected by a topology change but not its direction. As the density increases, the flow magnitude and its sensitivity to topology decreases.

Flows detected at the vertical probe location are generally weaker and show less sensitivity to plasma density. Yet, closer to the separatrix (figure 6), they recover the same trend as at the outer probe location. The weaker co-current flows detected by this probe in LSN and DN discharges may be partly an artifact of this probe's presheath extending close to the lower divertor surface at large $\rho$ (note the probe's proximity to the divertor in figure 1). Indeed, recent analysis of $C^{+2}$ impurity 'plumes' at this location (generated via $C_2D_4$ gas injection) [40] suggests such an effect to be present, which would cause this Mach probe to report a counter-current offset to the true value of $V_{\parallel\phi}$. The LSN data in figure 6 show a systematic decrease in $V_{\parallel\phi}$ with $\rho$ when $\rho > \sim 5$ mm, which is consistent with such an effect.

### *3.3. Poloidal flow information*

As illustrated in figure 8, the Mach probes only detect the parallel component of total plasma flow, $V_{\parallel\text{total}}$. This flow may consist of a combination of Pfirsch–Schlüter ion currents, $V_{\parallel\text{ps}}$, toroidal plasma rotation, $V_{\parallel\text{rot}}$, and a parallel component driven by cross-field transport, $V_{\parallel\text{trans}}$, arising to satisfy particle balance. An ionization-driven parallel flow may also be considered, although its relative contribution to the observed flow magnitude is expected to be small at locations far from the divertor [17]. Moreover, during 'puff and pump' experiments in JT-60U [20], which were designed to maximally affect flows in the SOL, only a 20% change or less in the measured parallel flow speeds were seen. Note that depending on the cross-field component ($E_r \times B$ flow), a strong parallel flow could be just the manifestation of a strong toroidal plasma rotation, $V_{\phi\text{rot}} \sim E_r/B_\theta$. In this case, there could be little or no net poloidal particle flux. Should this be happening on the inner SOL, our inference of strong parallel flows being driven by cross-field transport asymmetries would be incorrect. In the following subsections, we assemble information on poloidal flows in the C-Mod SOL with an eye towards re-constructing the total flow pattern.

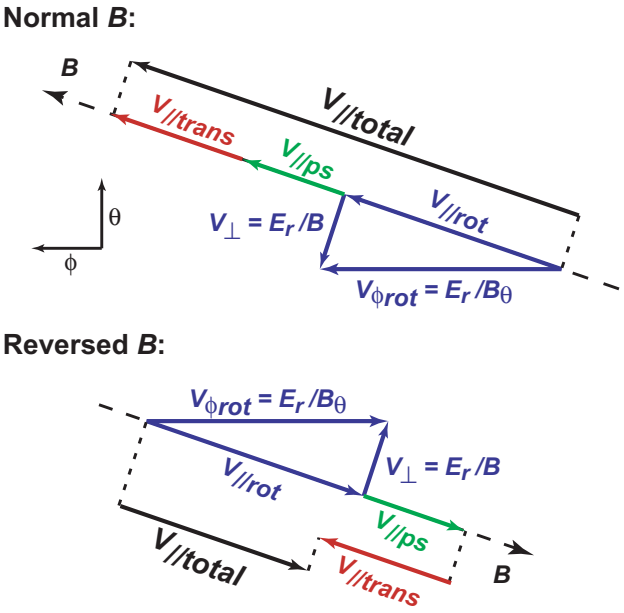


**Figure 8.** Magnetic fields and representative plasma flow components at the outer midplane, as viewed inwards along a major radius. Mach probes measure the total parallel flow ($V_{\parallel\mathrm{total}}$). Parallel flow components arising from Pfirsch–Schlüter ion currents ($V_{\parallel\mathrm{ps}}$) and toroidal rotation ($V_{\parallel\mathrm{rot}}$) reverse when $B_\mathrm{T}$ and $I_\mathrm{p}$ are reversed. In contrast, parallel flow components driven by cross-field transport ($V_{\parallel\mathrm{trans}}$) are expected to be insensitive to field direction but possibly dependent on X-point location (particularly in the high-field SOL), if the cross-field transport exhibits a strong ballooning-like character. Other flows, such as those arising from ionization imbalances, are omitted for clarity.

*3.3.1. Impurity plumes.* In a series of experiments aimed at studying flows near limiter and divertor surfaces, gaseous impurities were injected and low charge states of the resultant impurity plumes were imaged using a CCD camera with appropriate bandpass filters [41]. As shown by the representative $C^{+1}$ plumes in figure 9, the dispersion indicated a strong plasma flow and a clear dependence on X-point location, matching the flow behaviour seen in figure 5. Moreover, with discharge conditions and LSN/USN equilibria very similar to the data in figure 5, the strong flow was found to be persistently directed towards the inner divertor strike-point, independent of the discharge density and independent of the direction of $I_\mathrm{p}$ and $B_\mathrm{T}$ (which were reversed together). Unfortunately, the impurity gas injection rate used in these experiments was large enough to perturb locally the plasma conditions, excluding a reliable estimate of the local plasma flow velocity from the impurity dispersal. However, the pattern does show the total

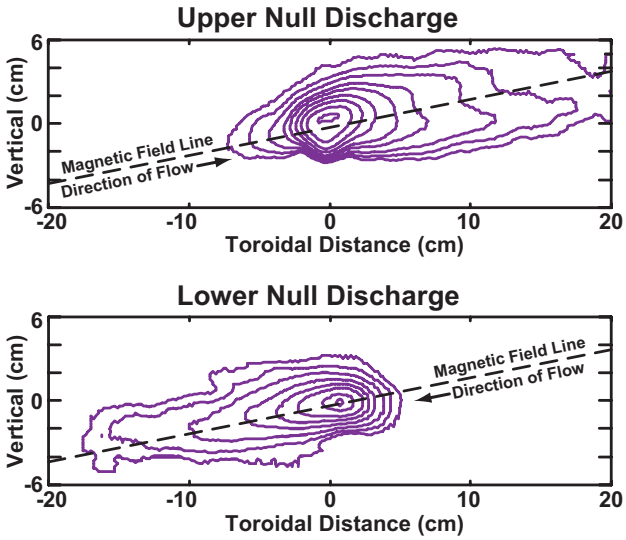


**Figure 9.** Contour plots of $C^{+1}$ dispersal (515 nm light, viewed along major radius direction) resulting from $CH_4$ injection at the inner wall, midplane location [41]. These data show strong plasma flow directed primarily along field lines in the inner SOL, with a clear dependence on LSN/USN topology.

flow vector to be closely aligned with the local magnetic field. Thus, the plumes provide strong evidence for parallel flows dominating over toroidal flows in the inner SOL. Additionally, the plumes clearly illustrate the effect of SOL flows on impurity migration: impurities born at the inside midplane wall migrate towards the inner divertor strike-point, regardless of the single-null X-point location.

*3.3.2. Effect of reversed B.* In contrast to the inner SOL, the data in figure 5 suggest that the $V_{\parallel\phi}$ in the outer SOL are more indicative of toroidal rotation and/or Pfirsch–Schlüter flows; $V_{\parallel\phi}$ there are less sensitive to X-point geometry and persistently co-current directed at low densities. In order to examine this trend further, electron pressure and parallel Mach number profiles from a series of matched LSN discharges ($0.5 < I_\mathrm{p} < 1.0\,\mathrm{MA}$, $4 < B_\mathrm{T} < 6\,\mathrm{T}$, $0.8 < \bar{n}_\mathrm{e} < 2.4 \times 10^{20}\,\mathrm{m}^{-3}$) with forward and reversed magnetic fields are shown in figure 10. Under the assumption that transport-driven parallel flows do not change, a comparison of forward and reversed-field discharges uncovers the contributions from toroidal rotation and/or Pfirsch–Schlüter flows (figure 8). Profile data are binned and colour-coded according to discharge density normalized to Greenwald density [42], $n/n_\mathrm{G}$, a parameter that is found to correlate with the character of transport and the behaviour of profiles in the plasma edge [39]. Positive (negative) Mach numbers in the 'normal $B$' ('reversed $B$') case indicate a co-current $V_{\parallel\phi}$. In response to field reversal, $V_{\parallel\phi}$ exhibits a roughly symmetric reversal near the outer midplane, suggesting that the relative contribution of $V_{\parallel\mathrm{trans}}$ to the total flow is small. There are some differences, however, which may relate to differences also seen in the electron pressure profiles (e.g. via changes in Pfirsch–Schlüter ion flows that are proportional to ion pressure gradients).

*3.3.3. Radial electric fields.* In principle, the radial electric field, $E_r$, can be estimated from the probe-inferred plasma

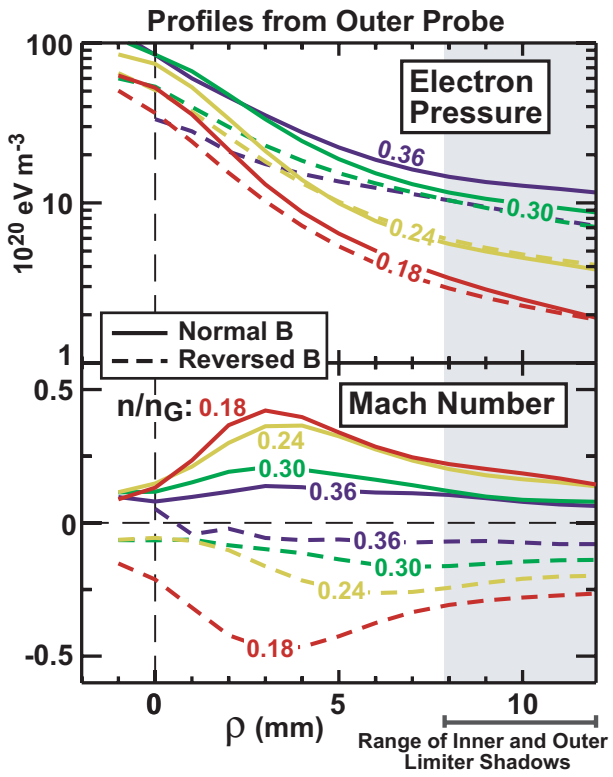


**Figure 10.** Comparison of outer probe electron pressure and Mach number profiles for forward and reversed magnetic field ($I_p$ and $B_T$ aligned). The parallel Mach flow is found to remain in the direction of $I_p$ (positive for normal $B$, negative for reversed $B$).

potential profile, $\Phi_{ps}$, and the resultant $E_r \times B$ component of plasma flow directly computed. This method involves adding an estimate of the sheath potential drop ($\sim 2.8T_e$) to the probe's floating potential [43]. However, we have found inconsistencies between $E_r$ inferred from this method and from two other methods: the poloidal propagation of plasma fluctuations [11] and the dispersal of impurity ions from a local gas puff [40]. These inconsistencies may be specific to our probe construction and/or the conditions found in C-Mod but likely involve plasma–surface effects, particularly those that influence secondary electron emission (affecting floating potentials and sheath potential drops). An additional complication, which is evident in the data of figures 2–4, is that a probe's floating potential depends on whether it is facing up or facing down. While such an effect is expected in a flowing plasma, the ambiguity further brings into question the accuracy of $E_r$ computed from these quantities, particularly since it involves taking the spatial gradient.

In view of these uncertainties, we treat $\Phi_{ps}$ as providing only qualitative information and avoid computing $E_r$ from this quantity since the inferred magnitude (and even sign) could be wrong! However, it is reasonable to consider that as long as the conditions near a probe ($n$, $T_e$, $|M_\parallel|$) remain approximately the same, a change in $\Phi_{ps}$ arising from a change in topology should mimic the change in true $\Phi$. With these ideas in mind, we plot the $\Phi_{ps}$ profiles from the three probes in figure 11. The discharges correspond to those of figure 5, and a similar binning of the data has been performed. The algebraic average of the up/down floating potentials is used (although not justified!), and the effect of electron-induced secondary electron emission from tungsten [44] is included.

Taken together, the data in figure 11 show a persistent trend: $\Phi_{ps}$ near the separatrix is most positive in LSN discharges, least positive in USN, and somewhere between in DN discharges. (However, note that $\Phi_{ps}$ obtained by the inner probe are up to $\sim$50 V different from those of the other two probes, justifying the level of caution stated here.) The data also suggest that $E_r$ at a location of $\rho = \sim 3$ mm becomes progressively more positive in the sequence USN, DN, LSN. Note that a toroidal rotation associated with $E_r$ would correspondingly increase in the co-current direction in the sequence USN, DN, LSN, a behavior that is consistent with the outer probe $V_{\parallel\phi}$ data in figures 5 and 7.

*3.3.4. Poloidal phase velocity of plasma fluctuations.* Previously, the contribution of toroidal plasma rotation to parallel flows near the outer midplane of Alcator C-Mod was studied for normal and reversed field discharges with a fixed, LSN topology [11]. Here, we extend the analysis to the discharges of figures 5 and 10, which include LSN, DN and USN topologies. In this analysis, the $E_r \times B$ drift velocity of the plasma, $V_{E\times B}$, is estimated from the poloidal phase velocity of plasma fluctuations, $V_{ph}$. (Some words of caution are also appropriate here. While fluctuation-induced cross-field fluxes inferred by probes may be corrupted by the plasma flux collected by the probe body [45], we are assuming here that the inferred $V_{ph}$ are still characteristic of the unperturbed plasma. In addition, $V_{ph}$ in this context may only be meaningful in regions where the plasma is not broken up into 'blobs' [37, 39], i.e. near the separatrix). Plasma fluctuations are expected to propagate with a superposition of $E_r \times B$ and drift-wave velocities (e.g. [46]), $V_d$,

$$V_{E\times B} = V_{ph} - V_d, \qquad V_d \approx \frac{T_e}{B}\frac{\nabla_r n}{n} + \alpha \frac{\nabla_r T_e}{B}. \quad (1)$$

The parameter '$\alpha$' accounts for finite electron temperature fluctuations and is expected to be of the order of $\tilde{T}_e n/\tilde{n} T_e$. Fluctuation data [47, 48] suggest this parameter may be near unity in the SOL. Nevertheless, we treat $\alpha$ as an adjustable parameter, $\alpha = 0$–1. In figure 12, the *poloidal* projections of parallel flow velocity, $V_{\parallel\theta}$, from the outer and vertical probes are plotted versus the corresponding *poloidal* fluid velocities ($\approx V_{E\times B}$), computed from equation (1). Good estimates of $V_{ph}$ are obtained at this location ($\rho = 4$ mm), and a value of $\alpha = 1$ has been used. The discharges include those of figures 5 and 10 but are restricted to those with $|I_p| = 0.8$ MA and $|B_T| = 5.4$ T.

A clear correlation between the two velocities is exhibited in figure 12. For the case of the outer probe, the data fall close to the dashed line that corresponds to a condition of pure toroidal rotation, $V_{\phi rot} \sim E_r/B_\theta$, i.e. the poloidal projections of parallel and $E_r \times B$ flows approximately cancel. Data from the vertical probe do not track the dashed line. For LSN and DN discharges, this might be explained by the presheath effect noted earlier in section 3.2; $V_{\parallel\theta}$ inferred from this probe may be biased towards smaller positive values. However, the USN data (where presheath effects should be absent) also fall below the dashed line. In the USN topology, a net poloidal flow of plasma from the low- to the high-field side is suggested, in this case driven by $E_r \times B$ flows.

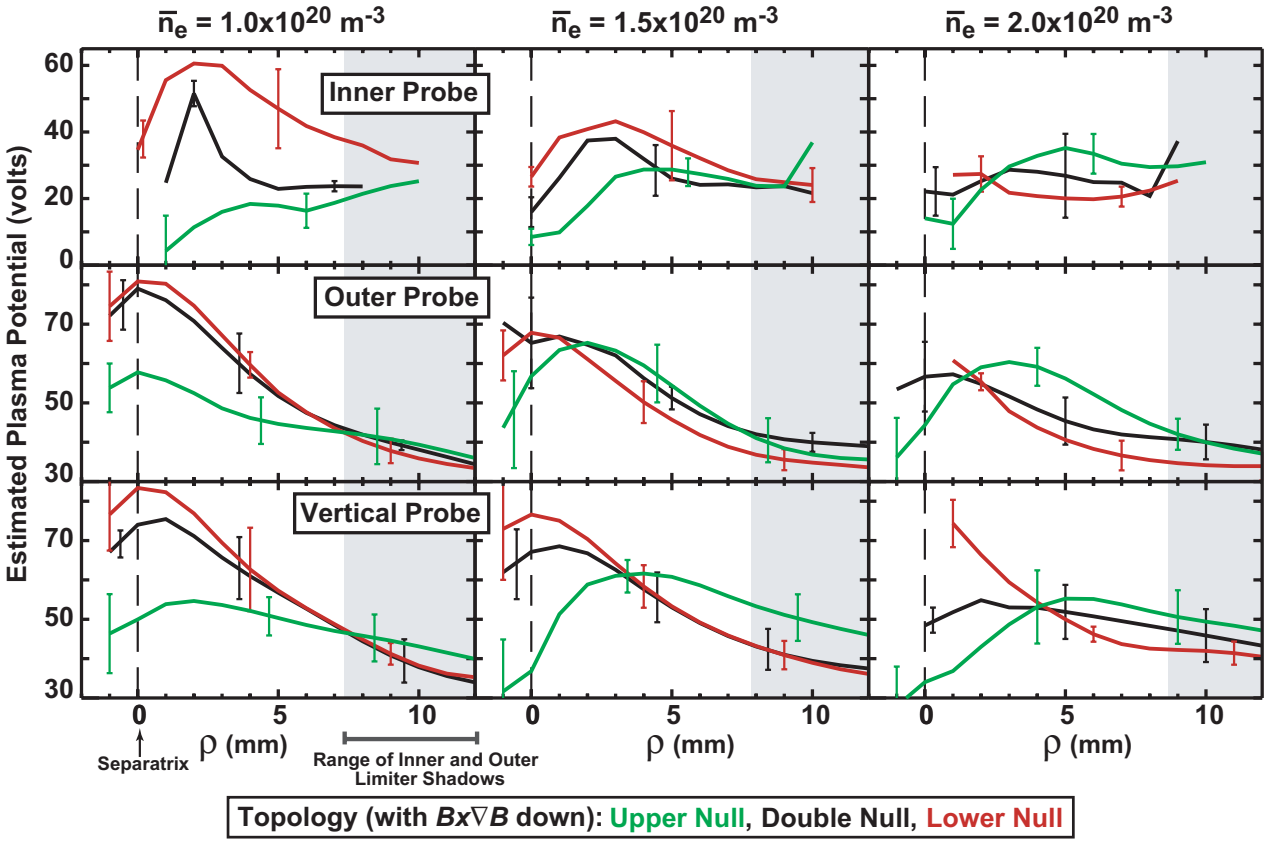


**Figure 11.** Probe-sheath estimated plasma potential profiles. Data are for the same set of discharges represented in figure 5.

The above inferences are sensitive to the assumed value of $\alpha$. As $\alpha$ is reduced, the magnitude of $V_{E\times B}$ computed from equation (1) becomes smaller. Consequently, $V_{\|\theta}$ becomes uncompensated by the (estimated) $E_r \times B$ flows and an increasingly larger net poloidal flux is inferred, directed upwards (downwards) in forward (reversed) magnetic field cases. Note that at the outer midplane, the component of $V_{\|\theta}$ arising from a Pfirsch–Schlüter ion flow (in a reference frame rotating toroidally, $V_\phi = E_r/B_\theta$) can be estimated as

$$V_{\|\theta}^{\mathrm{PS}} \approx -2\varepsilon \frac{\nabla p_\mathrm{i}}{nB} \sim -2\varepsilon \frac{\nabla T_\mathrm{e}}{B}, \qquad (2)$$

where $\varepsilon$ is the inverse aspect ratio, $a/R$. Thus, if we reduce $\alpha$ from 1 to $1 - 2\varepsilon \sim 0.4$, a re-plot of the outer probe data in figure 12 would show $V_{\|\theta}$ in excess of pure toroidal rotation (dashed line) and this excess would, by construction, correspond to a Pfirsch–Schlüter ion flow. Therefore, two principal conclusions follow from these observations: (1) experimental uncertainties prevent us from unfolding separate contributions to $V_{\|\phi}$ from toroidal rotation and Pfirsch–Schlüter ion flows and (2) yet a combination of these two effects can largely account for the observed values of $V_{\|\phi}$ in the outer SOL.

### *3.4. Flow observations summary*

In summary, the data from the inner SOL exhibit clear and consistent results: a strong parallel plasma flow directed from the low- to the high-field SOL regions when field lines connect between the two. The principle drive mechanism is connected to a strong poloidal asymmetry in the cross-field transport. Parallel flows measured by the inner Mach probe do not reverse symmetrically with X-point reversal. This may be caused by inaccuracies in this probe's projected area and/or the presence of Pfirsch–Schlüter ion flows, such as those suggested in the flow measurements on the inner divertor leg of JT60-U [20]. The data on the outer SOL also exhibit clear trends under magnetic field and X-point reversal; parallel flows are consistent with some combination of toroidal rotation and Pfirsch–Schlüter effects playing a leading role. Using this information as a guide, we now turn towards a flux-tube model to analyse the transport-driven components of the parallel flow and to construct an estimate for the ballooning-like transport asymmetry that appears to drive them.

## 4. Analysis: transport-driven parallel flows

The data in figure 5 were taken from discharges that utilized a nearly mirror-symmetric reflection of flux surface shape in going from LSN to USN. Here we exploit these symmetries to expose the transport-driven component of the parallel flow, i.e. parallel flow arising from cross-field transport and particle balance constraints. As shown in figure 8, $E_r$-driven toroidal rotation and Pfirsch–Schlüter components of parallel flow change sign upon $B$ reversal, while transport-driven parallel flows are expected to retain the same sign. Thus transport-driven flow components can be estimated simply by averaging measurements from the forward and reversed

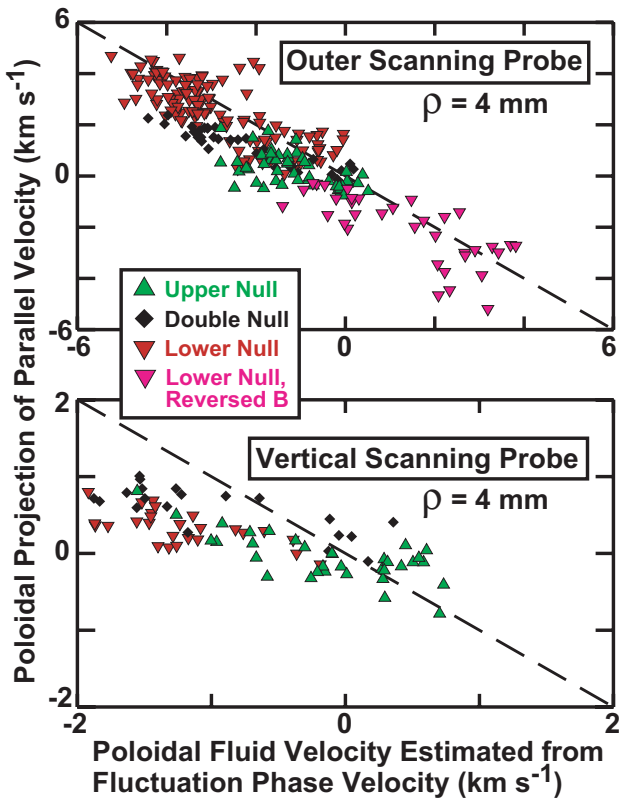


**Figure 12.** Poloidal projection of parallel flow versus poloidal fluid velocity estimated from fluctuation propagation, under the assumption that $\alpha = 1$ (see text). A positive velocity indicates a flow directed upwards. The dashed line corresponds to a condition of pure toroidal rotation.

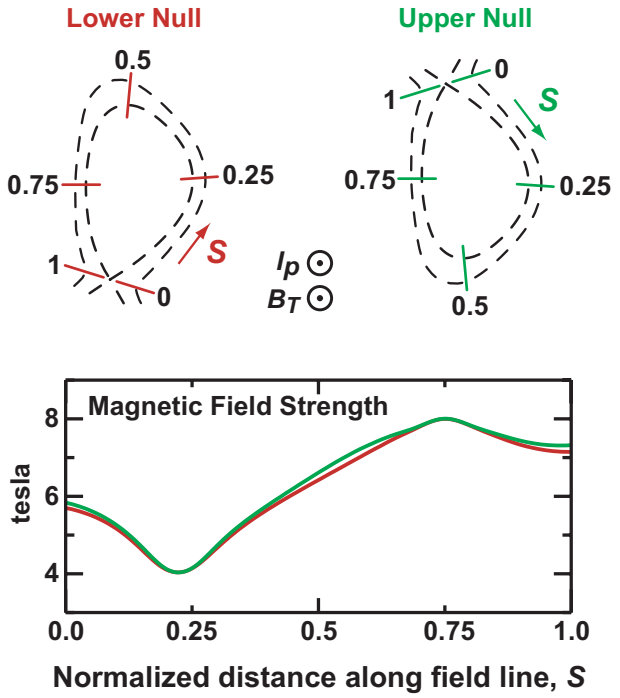


**Figure 13.** Definition of the flux-tube coordinate, $s$, in LSN and USN discharges. The flux surface shapes are similar when mirrored up/down, as shown by overlaying magnetic field strengths from the $\rho = 4$ mm flux surface.

$B$ directions. If we assume that the divertor geometry does not influence significantly the flows seen outside the divertor region (a reasonable assumption, based on the similarities among the flows here and those seen in JT-60U [10], JET [9] and TCV [12], devices with significantly different divertor geometries), then we can apply the same technique to the set of matched LSN and USN discharges with fixed $B$ direction (figure 5); we need only map the USN data onto the LSN equilibria by mirror-reflecting the flux surfaces and applying a minus sign to the USN flow velocities.

### *4.1. Flux-tube mapping*

In a toroidally symmetric system, the quantities on a magnetic flux surface can be mapped to the distance along field lines, $s$, as illustrated in figure 13. This 'flux-tube coordinate' is normalized to have values running from 0 to 1 as the tube transits from the outer to the inner divertor legs, starting near the X-point. Velocities directed along increasing $s$ are defined as positive. As an example, the magnetic field strength is plotted versus $s$, also illustrating a good match between LSN and USN equilibria. An additional benefit of mapping the flow data to this coordinate system is that any systematic offsets in $M_\parallel$ (arising from unequal up/down probe areas, for example) will change sign in switching from LSN to USN. Therefore, a simple averaging of data will yield a good estimate of the transport-driven flow component.

Figure 14 shows an example of probe-inferred plasma parameters (at $\rho = 4$ mm) mapped onto this coordinate system. The data are from the same set of discharges as in figure 5, binned into three density groupings (colour-coded). The symbols represent averaged values, while the vertical bars indicate $\pm 1$ standard deviation. These flux-tube plots clearly illustrate features noted earlier: lower electron pressures, lower $T_e$ values and near-sonic parallel flows on the inner SOL. As anticipated, the $M_\parallel$ data exhibit two components: (1) a persistent trend of parallel plasma flow from the outer to the inner SOL (the transport-driven component that we are seeking) and (2) systematic offsets about this trend that depend on the X-point location (some combination of toroidal rotation, Pfirsch–Schlüter ion flows and Mach-probe offset effects).

The increase in $M_\parallel$ with $s$ in figure 14 implies that there is a net source of particles into the flux tube, $S_{net}$; this source must account for the net loss of particles out of its ends. In the model described below, we consider the dual constraints of particle and parallel momentum balance in the flux tube. This will allow us to construct a plausible estimate of the magnitude and spatial structure of $S_{net}$, given the measured 'input values' of $M_\parallel$ (e.g. figure 14). Subsequently, we address the poloidal asymmetry in cross-field particle transport that is implied.

### *4.2. Flux-tube model*

Steady-state plasma fluid equations for particle continuity and parallel momentum balance [49] can be written as

$$\nabla \cdot nv = S_p, \tag{3}$$

$$m_i n \tfrac{1}{2} \nabla_\parallel v_\parallel^2 + \nabla_\parallel p \approx m_i n [(v_\parallel \cdot \nabla_\parallel) v]_\parallel + \nabla_\parallel p$$
$$= -m_i n [(v_\perp \cdot \nabla_\perp) v]_\parallel - (\nabla \cdot \pi_i)_\parallel - R_{\parallel ni} - m_i v_\parallel S_p, \tag{4}$$

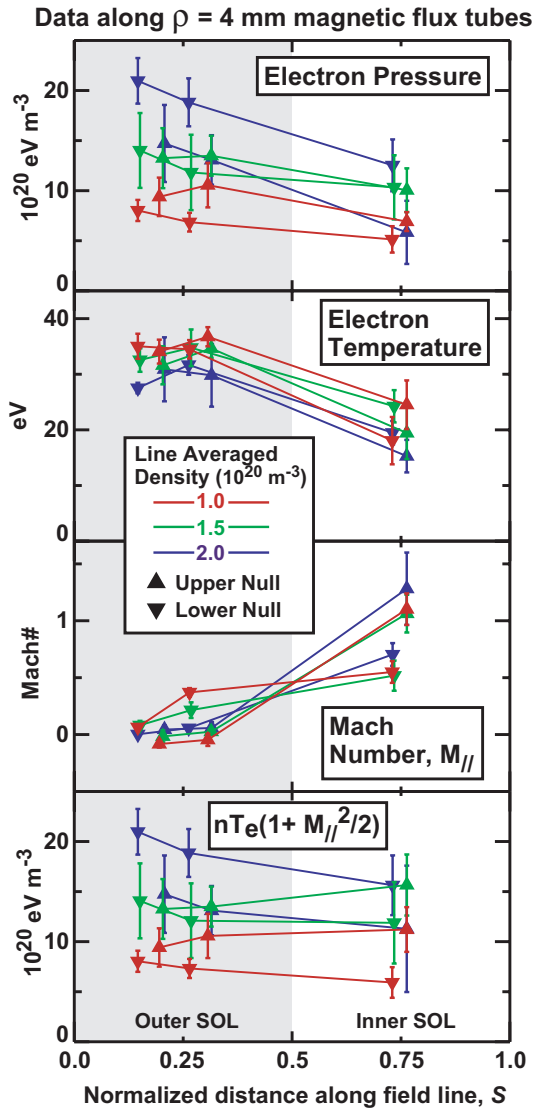


**Figure 14.** Plasma conditions at three scanning probe locations plotted versus flux-tube coordinate, $s$, at the $\rho = 4$ mm flux surface. Straight lines connecting symbols are included to guide the eye.

where $S_\mathrm{p}$ is the rate of ionization minus recombination and $R_{\parallel\mathrm{ni}}$ is the rate of momentum transfer to the neutral species. For simplicity, the electron and ion species are assumed to be sufficiently self-collisional to be Maxwellian with temperatures $T_\mathrm{i}$ and $T_\mathrm{e}$. Lacking information on $T_\mathrm{i}$, we further approximate $T_\mathrm{i} \approx T_\mathrm{e}$. (Note: The isotropization time for ions can be larger than the parallel flow time from the outer to inner midplane, suggesting that a bi-Maxwellian description with appropriate modification to the ion fluid momentum equation, e.g. [50], would be more precise.) The right-hand side of equation (4) contains parallel momentum source/sink terms. Parallel momentum transfer via turbulence (Reynolds stress, e.g. [51]) could also be included. The most relevant question to address is: Are these terms significant? The data in figure 14 suggest that the density varies weakly along $s$. Therefore, the left-hand side of equation (4) can be approximated as

$$\mathrm{LHS} \approx 2\nabla_\parallel \left[ nT_\mathrm{e} \left( 1 + \frac{1}{2} M_\parallel^2 \right) \right]. \tag{5}$$

The bracketed term is plotted in the bottom panel of figure 14. Only a relatively small variation in this quantity is evident (highest density case). Therefore, a good first-approximation is to treat the aggregate of terms on the right-hand side of equation (4) as being small. (Momentum losses in the divertor regions can in fact be quite high, e.g. plasma detachment, but those regions are excluded here.) While we see that the sum of thermal and parallel flow energy densities is approximately constant along the flux tube, a trade-off between them obviously occurs.

Note that in order to satisfy equation (3), the parallel flux density must be of the form

$$nv_\parallel = BL_{xx} \int \frac{S_\mathrm{p} - \nabla \cdot nv_\perp}{B} \partial s, \tag{6}$$

where $L_{xx}$ is the length of a field line spanning from $s = 0$ to 1. Equation (6) exhibits the following behaviour: wherever the net particle source, $S_\mathrm{net} = S_\mathrm{p} - \nabla \cdot nv_\perp$, is zero along a section of flux tube, the parallel flux density, if it is non-zero, will vary in proportion to the local magnetic field strength. This response is expected. As with the magnetic field, the flux density times the cross-sectional area of the flux-tube must remain constant where $S_\mathrm{net}$ is zero. Such a 'nozzle effect' can be important. As seen in figure 13, the magnetic field strength varies by a factor of 2 along $s$. Therefore, a moderate parallel flow at the outer midplane can transform into a near-sonic parallel flow at the inner midplane. Integrating equation (6) from $s = a$ to $b$, one obtains the relationship between Mach number ($M_\parallel$), density ($n$) and sound speed ($C_\mathrm{s}$) at these two locations and the net particle source profile between,

$$M_{\parallel b} = \frac{n_a C_{sa}}{n_b C_{sb}} B_b \left[ \frac{M_{\parallel a}}{B_a} + \frac{L_{xx}}{n_a C_{sa}} \int_a^b \frac{S_\mathrm{net}}{B} \partial s \right]. \tag{7}$$

A more convenient form is

$$M_{\parallel b} = \frac{n_a C_{sa}}{n_b C_{sb}} B_b \left[ \frac{M_{\parallel a}}{B_a} + c \int_a^b \frac{f}{B} \partial s \right], \tag{8}$$

with the definitions

$$cf(s) = \frac{S_\mathrm{net} L_{xx}}{n_a C_{sa}}, \qquad \int_a^b f \partial s = 1. \tag{9}$$

The function, $f(s)$, specifies the shape of $S_\mathrm{net}$, while the constant, $c$, specifies its magnitude relative to a characteristic plasma loss rate, $n_a C_{sa}/L_{xx}(b-a)$.

Note that equation (8) is defined rigorously; it is just a different form of the particle continuity equation. Our goal is to use equation (8) to compute $M_\parallel$ along $s$ with different 'trial functions' for $f(s)$ and compare the results with measurements of $M_\parallel$. However, we must account for a variation of $nC_\mathrm{s}$ along field lines. In principle, a model could be constructed for this variation using the additional constraints of parallel momentum conservation and energy transport. However, such an approach would be inherently unreliable since it involves unknown quantities such as cross-field heat transport and its poloidal variation. Instead, turning to the measurements (e.g. figure 14), we find that the quantity $nC_\mathrm{s}$ varies weakly along field lines; it decreases by a factor of ~0.7 in going from the

outer to the inner SOL. A simple variant of equation (8) that approximately accounts for this behaviour is

$$M_{\|b} = \mathrm{e}^{(M_{\|b}^2 - M_{\|a}^2)/2} B_b \left[ \frac{M_{\|a}}{B_a} + c \int_a^b \frac{f}{B} \partial s \right]. \qquad (10)$$

The exponential pre-factor evaluates to 1/0.7 for $M_{\|a} = 0$ and $M_{\|b} = 0.84$, numbers that are comparable with those measured at the outer and inner SOL regions (figure 14). Moreover, the basis for equation (10) is of theoretical interest. This formula is rigorously correct in a plasma where $T_\mathrm{e}$ and $T_\mathrm{i}$ are constant along field lines and where the rhs terms of equation (4) can be neglected,

$$\nabla_\| \left[ \ln(n) + \frac{M_\|^2}{2} \right] = 0. \qquad (11)$$

In such a system, the trade-off between thermal and parallel flow energy densities involves the plasma density alone. Thus, we adopt equation (10) as a reasonable model equation for the present discussion, recognizing that it also can extend to situations beyond the immediate problem at hand.

### *4.3. Flux-tube particle source profiles*

With the help of equations (9) and (10), we consider the following questions: (1) Can the parallel flow measurements be quantitatively matched for some reasonable net source profile? (2) If so, what is its spatial variation? (3) What is the magnitude of the implied cross-field transport?

The answers to questions (1) and (2) are contained in figure 15. Measured values of $M_\|$ at $\rho = 2$, 4 and 6 mm (triangles) are shown for matched LSN/USN discharges. Values midway between these (but not greater than $M_\| = 0.95$, to avoid the supersonic branch in the model equations that occurs at $M_\| = 1$) are taken as the 'transport-driven' components of the parallel flow (x symbols). The shape of the net source, $f(s)$, and its magnitude, $c$, are adjusted until $M_\|(s)$ from equation (9) closely matches the 'data points'. Resultant $S_\mathrm{net}$ profiles are shown as dashed curves in figure 15. While the solutions are not unique, they clearly demonstrate that a quantitative match to plasma flow measurements can be obtained for $f(s)$ profiles similar to the ones shown. The solutions also show the type of poloidal asymmetry that is required of $S_\mathrm{net}$, which is expected to be closely related to the spatial variation of cross-field transport fluxes. (However, these quantities are not necessarily proportional; see below.)

### *4.4. Plasma circulation and cross-field transport asymmetries*

Note that a steady-state plasma flow loop is implied by the results shown in figure 15: excess plasma enters flux tubes near the outer SOL; a large fraction of this flows along field lines to the inner SOL and presumably neutralizes at or near the inner divertor surface (via surface or volume recombination). In order to close the loop, neutrals likely ionize inside the separatrix near the inner divertor leg; the resulting ions are free to over-populate flux tubes in the outer SOL once again. (Another possible but unlikely scenario is the convection of plasma, rather than neutrals, inside the separatrix near the inner divertor.) It is important to note that neutral ionization in the outer SOL, $S_\mathrm{p}$, is not part of this flow loop. Although a large ionization source is indeed found in the outer SOL of Alcator C-Mod, it is primarily associated with a different flow loop: one of cross-field transport onto main-chamber wall surfaces and associated recycling [52].

In light of these considerations, the net particle source can be approximated as

$$S_\mathrm{net} = S_\mathrm{p} - \nabla \cdot n v_\perp \approx \left( S_\mathrm{p} - \frac{\partial\, n v_r^\mathrm{mc}}{\partial r} \right) - \frac{\partial\, n v_r^\mathrm{so}}{\partial r} \approx - \frac{\partial n v_r^\mathrm{so}}{\partial r}, \qquad (12)$$

where $S_\mathrm{p}$ is balanced primarily by the radially increasing plasma fluxes associated with main-chamber recycling, $n v_r^\mathrm{mc}$. The flux, $n v_r^\mathrm{so}$, is the only component that is truly 'scraped off'; this flux yields an excess of particles that must be 'drained' by parallel flows to the divertors. The spatial profiles of $S_\mathrm{net}$ shown in figure 15 can therefore be viewed as representing the quantity $n v_r^\mathrm{so}/\lambda_n$, where $\lambda_n$ is a characteristic density gradient scale length. However, since $n v_r^\mathrm{so}$ is only part of the total cross-field flux, the spatial variation in $S_\mathrm{net}$ does not necessarily indicate the spatial variation in total cross-field transport, $n v_r^\mathrm{total}$; the main-chamber recycling flux must also be included.

In the low-density discharges of figure 15, $S_\mathrm{net}$ exhibits a classic ballooning structure—peaked near the outer midplane. In these discharges, the ratio of main-chamber to divertor recycling is the lowest. Therefore, the spatial variation of $S_\mathrm{net}$ may be indicative of the underlying poloidal asymmetries in the cross-field transport fluxes, $n v_r^\mathrm{so} \propto n v_r^\mathrm{total}$. However, as the plasma density is raised, the peak in $S_\mathrm{net}$ offsets in a direction towards the inner divertor. Although one cannot rule out the possibility that the poloidal asymmetry of the underlying transport has correspondingly changed, the shift in $S_\mathrm{net}$ is more likely related to the increase in main-chamber recycling that is observed at higher densities [52]. The same ballooning-like poloidal structure may still be present; it could be just that a larger fraction of the total cross-field flux near the outer midplane tends to exhaust onto main-chamber wall surfaces.

### *4.5. Magnitude of cross-field transport*

Our final task is to characterize the magnitude of $n v_r^\mathrm{so}$ and to relate it to results from previous transport analyses. A flux-tube averaged value of $n v_r^\mathrm{so}$ can be expressed in terms of the effective convection ($V_\mathrm{eff}$) and diffusion ($D_\mathrm{eff}$) coefficients,

$$\frac{n_a V_\mathrm{eff}}{\lambda_n} \equiv \left\langle - \frac{\partial n v_r^\mathrm{so}}{\partial r} \right\rangle \approx \frac{1}{b-a} \int_a^b S_\mathrm{net} \partial s = \frac{c}{b-a} \frac{n_a C_{sa}}{L_x}, \qquad (13)$$

$$D_\mathrm{eff} \equiv V_\mathrm{eff} \lambda_n,$$

where $n_a$ and $\lambda_n$ are the density and its e-folding length near the outer midplane. The interval $[a,b]$ corresponds to the flux-tube segment between probe measurements.

A compilation of $V_\mathrm{eff}$ and $D_\mathrm{eff}$ values is shown in table 1. The magnitudes are comparable with those obtained from earlier UEDGE modelling [53] and from SOL particle balance measurements [39, 52, 54] in similar discharges. These previous studies identified a systematic increase of cross-field transport with distance from the separatrix and with discharge density, a trend reproduced in table 1. Although the earlier studies were based on poloidally uniform

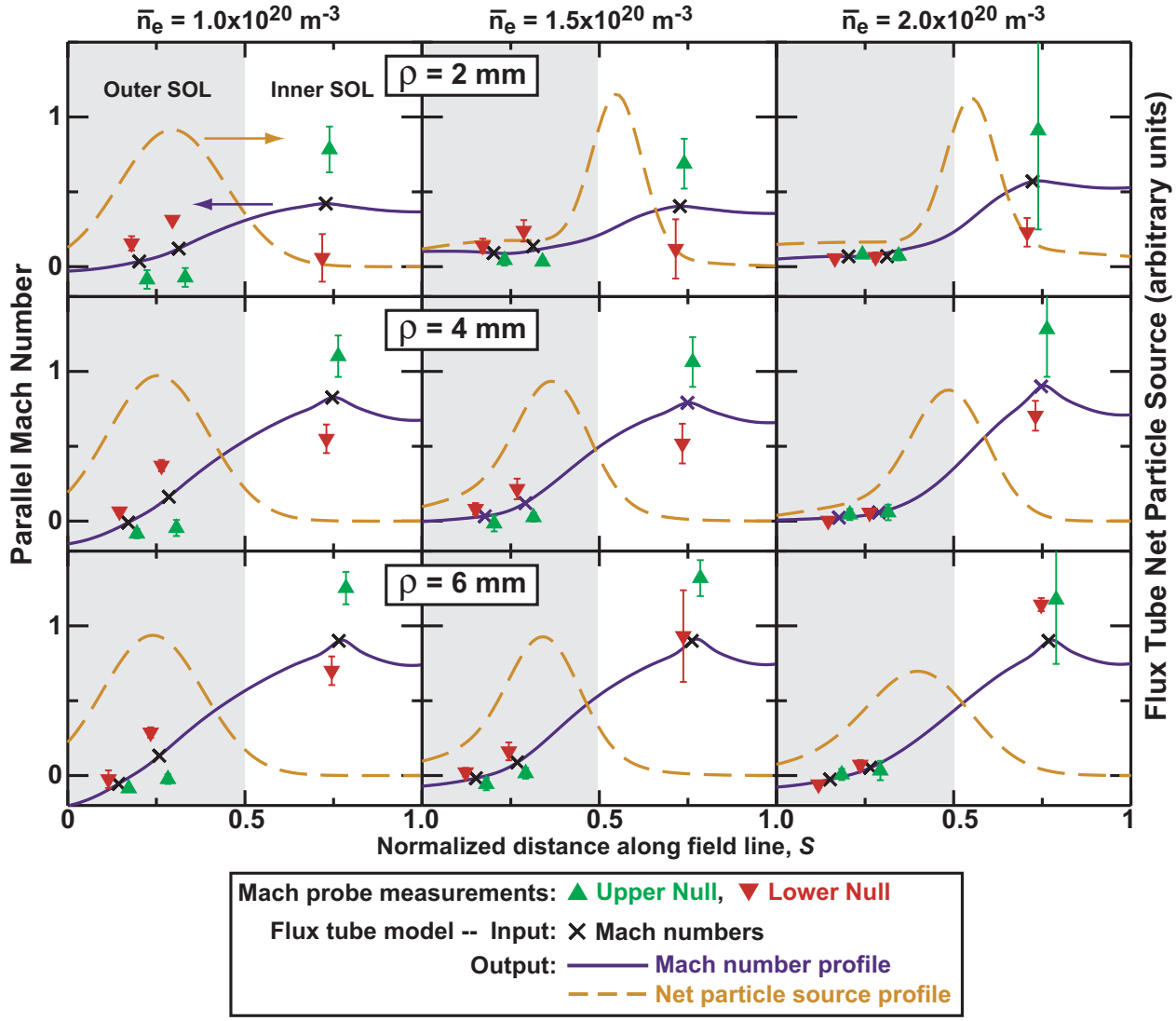


**Figure 15.** Results from parallel flow model (from same data set as figure 5).

**Table 1.** Flux-tube averaged cross-field transport coefficients corresponding to the net particle source profiles in figure 15.

| $\bar{n}_e$ ($10^{20}$ m$^{-3}$) | $\rho$ (mm) | $c$ | $V_{\text{eff}}$ (m s$^{-1}$) | $D_{\text{eff}}$ (m$^2$ s$^{-1}$) |
|---|---|---|---|---|
| 1.0 | 2 | 0.20 | 7.7 | 0.06 |
| | 4 | 0.36 | 14 | 0.15 |
| | 6 | 0.42 | 19 | 0.32 |
| 1.5 | 2 | 0.16 | 7.2 | 0.07 |
| | 4 | 0.34 | 15 | 0.19 |
| | 6 | 0.41 | 16 | 0.23 |
| 2.0 | 2 | 0.29 | 18 | 0.27 |
| | 4 | 0.42 | 28 | 0.56 |
| | 6 | 0.45 | 32 | 0.84 |

transport coefficients—a situation clearly contrary to the new information here—the principal conclusions appear to remain valid. We anticipate that the main effects of properly accounting for poloidal transport asymmetries in SOL models would be (1) reproduction of observed plasma flow patterns, including the strong flows in high-field SOL, (2) more accurate inference of cross-field transport coefficients and (3) determination of the topology-dependent flow boundary conditions imposed by the SOL on the confined plasma.

## 5. Topology-dependent flow boundary conditions and plasma rotation

As a result of transport-driven parallel flows, the SOL plasma can develop a net volume-averaged toroidal momentum (illustrated in figure 16($a$)): co-current directed for $B \times \nabla B$ pointing towards the X-point and counter-current directed otherwise. An important question is, do these SOL flows affect the plasma inside the separatrix? Intuitively, we expect the confined plasma to react to these different flow boundary conditions with a change in its toroidal rotation—a reaction that incurs minimal resistance in this axisymmetric geometry. However, the magnitude of such a response would ultimately depend on the details of the momentum transfer mechanisms, in particular, their poloidal variation and sensitivity to the strong SOL flows that occur in the high-field region.

Exploring these ideas, the toroidal velocities measured near the separatrix from the three Mach probes ($V_{\|\phi}$) and in

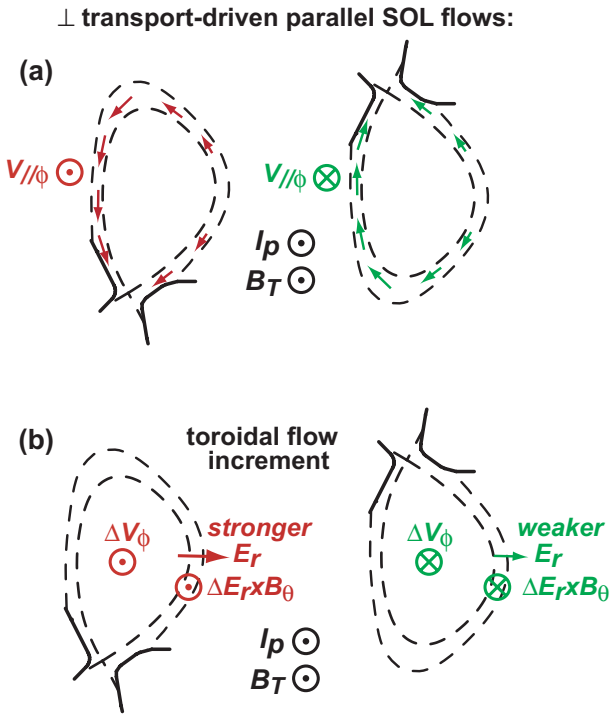


**Figure 16.** (*a*) Ballooning-like transport leads to a net volume-averaged SOL plasma momentum, co- or counter-current directed, depending on X-point location. (*b*) Data in figures 17 and 18 show that the confined plasma can react to this boundary condition with a positive (negative) increment in the co-current rotation when $B \times \nabla B$ is towards (away from) the X-point. Correspondingly, the toroidal rotation and radial electric fields in the SOL are influenced (as suggested from data in figure 11), becoming more (less) positive.

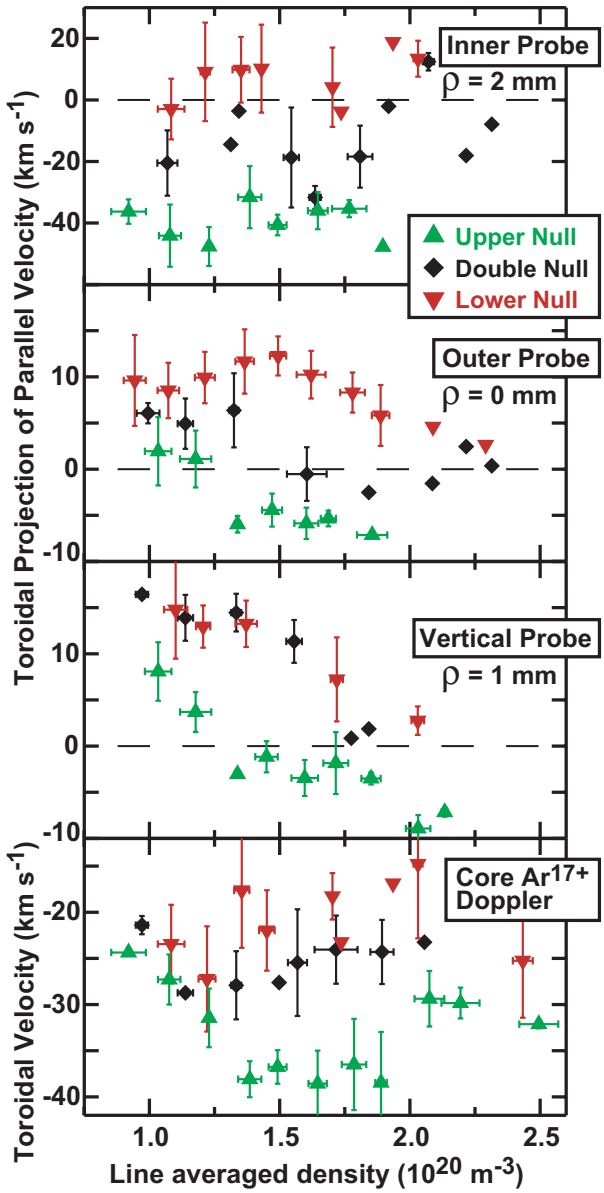


**Figure 17.** Toroidal projection of parallel plasma flow measured near separatrix by three scanning probes (top three panels) and corresponding toroidal velocity of central $Ar^{17+}$ ions (bottom panel). In changing from upper to lower null, a positive increment in toroidal velocity (co-current directed) is detected on all signals. Data points are binned with $\Delta\bar{n}_e \sim 0.14 \times 10^{20}\,m^{-3}$. Vertical bars indicate $\pm 1$ standard deviation.

the plasma centre from $Ar^{17+}$ ions are shown in figure 17. The data are binned and plotted versus $\bar{n}_e$. The discharge conditions were $I_p = 0.8\,MA$, $B_T = 5.4\,T$ and $B \times \nabla B$ pointing down. A remarkable correlation is revealed among the flow measurements: a co-current velocity increase of $\sim 15\,km\,s^{-1}$, detected by the outer and vertical probes in going from USN to LSN, is systematically matched by a comparable change in core plasma rotation. These topology-dependent increments in toroidal velocity also exhibit a similar trend to $\bar{n}_e$, becoming diminished at low densities. In contrast, the toroidal velocities detected at the inner probe location behave somewhat differently: they exhibit a factor of $\sim 3$ larger change towards the co-current direction in going from USN to LSN and display no sensitivity to $\bar{n}_e$.

These data suggest that topology-dependent SOL flows can indeed influence the confined plasma. The near-sonic flow on the inner SOL appears to be the source of the overall rotation drive; it is the largest velocity in the system and its change with topology is insensitive to discharge parameters. Apparently, the net coupling of this flow momentum into the confined plasma can vary with discharge conditions (e.g. $\bar{n}_e$).

In other discharges ($I_p = 0.8\,MA$, $B_T = 5.4\,T$, $\bar{n}_e = 1.5 \times 10^{20}\,m^{-3}$), we have explored the sensitivity of SOL flows and core plasma rotation to magnetic flux balance, parametrized here as the distance between primary and secondary separatrix mapped to the outer midplane (figure 18). These data independently indicate a close coupling between SOL flows and core rotation: the central and edge velocities (outer probe) are seen to have a proportionality of roughly $\sim 1.5$ in figure 18(*b*). The velocities also display a remarkable sensitivity to magnetic topology: a $\sim 5$ mm shift in the X-point balance is sufficient to completely reverse the flows. This size scale is comparable with the pressure gradient scale lengths near the separatrix (figure 5)—an expected result if in/out pressure asymmetries on open field lines are the principle drive mechanism.

Another interesting and testable consequence of the transport-driven toroidal rotation hypothesis is its feedback (via momentum transfer) on the SOL; the helical flow pattern should be partially converted into a toroidal rotation that

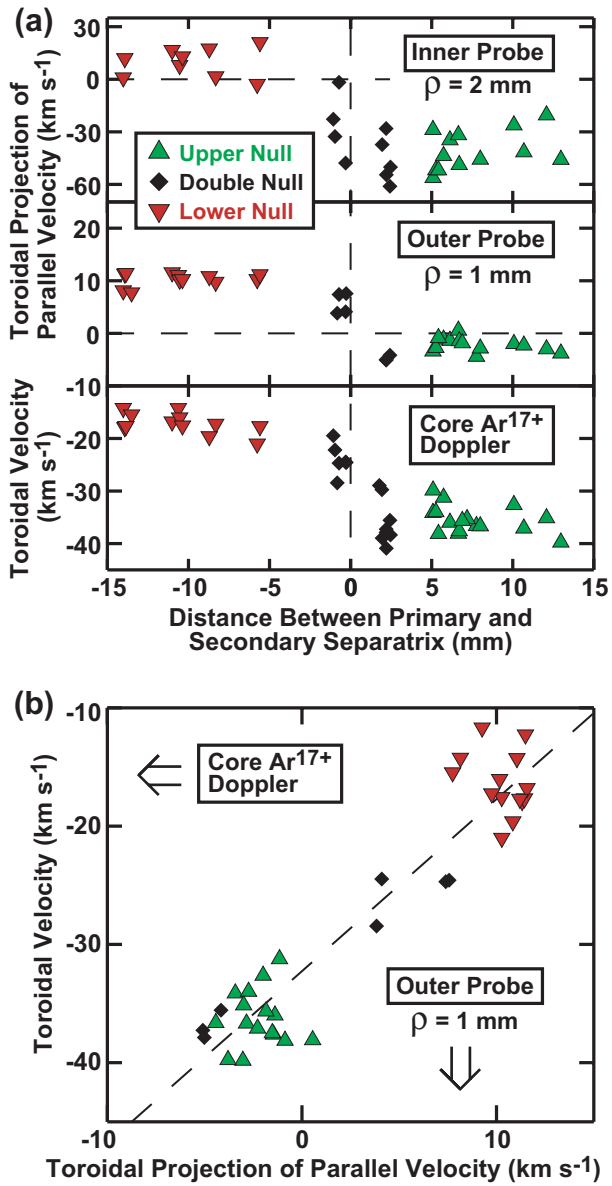


**Figure 18.** (*a*) Toroidal flow velocities as a function of magnetic flux balance between upper and lower X-point in otherwise identical discharges. (*b*) Toroidal velocity of central $Ar^{17+}$ ions versus toroidal projection of parallel flow measured by the outer probe, at a location 1 mm outside the separatrix. The fitted dashed line has a slope of 1.5.

mimics the confined plasma's response. Also, since the radial electric field is intimately connected to toroidal rotation, a correspondingly more positive (less positive) $E_r$ should be seen in the SOL for $B \times \nabla B$ pointing towards (away from) the X-point (see figure 16(*b*)). As discussed earlier, the data in figures 5 and 11 show precisely these tendencies: stronger co-current rotation and more positive $E_r$ in LSN, weaker co-current rotation and less positive $E_r$ in USN.

The latter observations are particularly intriguing. Radial electric field gradients and associated $E \times B$ velocity shear have been identified [55–57] for regulating cross-field transport: the L–H confinement mode transition is thought involve a bifurcation in plasma transport characteristics near the vicinity of the separatrix [58], triggered by the attainment of a certain level of velocity shear [59]. In addition, magnetic topology is well known to affect the L-H threshold [60]; generally, higher powers are required when $B \times \nabla B$ points away from rather than towards the active X-point. Yet, no compelling explanation for this behaviour has been advanced. The experimental results reported here point to a possible explanation: transport-driven SOL flows, modulated by magnetic topology, affect radial electric fields and, by inference, flow shear near the separatrix.

## 6. SOL flows, core plasma rotation and L–H threshold

We have recently investigated the effect of magnetic topology (LSN, DN, USN) on the L–H power threshold in Alcator C-Mod, with specific emphasis on SOL flows and toroidal rotation of the confined plasma. Strong circumstantial evidence has been found that supports the hypothesis advanced above, namely that transport-driven SOL flows set topology-dependent boundary conditions that influence the L–H transition.

The time-evolutions of three discharges that exhibited an L–H transition are shown in figure 19. Prior to application of ICRF power, these Ohmic L-mode target plasmas had similar external control parameters ($I_p = 0.8$ MA, $B_T = 5.4$ T, $\bar{n}_e = 1.4 \times 10^{20}\,m^{-3}$, $B \times \nabla B$ down) but different magnetic topologies (USN, DN, LSN). Electron temperatures measured by ECE and edge Thomson scattering [61] as well as electron pressure gradients near the 95% magnetic flux surface are nearly identical in the Ohmic L-mode phases. A similar observation has been noted on DIII-D; edge profiles remained unchanged in switching from LSN to USN [62]. However, important differences are revealed here in the core rotation during the Ohmic phase, stepping from $\sim -50$ to $-30$ to $0\,km\,s^{-1}$ in the sequence USN, DN, LSN. As discussed above and shown in figures 17 and 18, this behaviour can be understood in terms of the boundary conditions imposed by SOL flows. Therefore, despite superficial similarities, the target plasma conditions are in fact fundamentally different, e.g. topology-dependent toroidal rotation and associated electric fields near the separatrix.

ICRF heating power is applied at levels close to the L–H threshold (0.9, 1.6, 2.9 MW) to yield a transition later in time. This power is from 2 two-strap antennae (80 MHz, $0 - \pi$ phasing) and one four-strap antenna (78 MHz, $0 - \pi - 0 - \pi$ phasing) using a hydrogen minority heating scenario. It is important to note that this heating method imparts no direct momentum input to the plasma. In response to the RF power, edge electron temperatures and pressure gradients evolve, most notably for high input powers (USN). At the time of L–H transition, the edge electron temperature is approximately a factor of 2 higher in the USN case; pressure gradients are correspondingly higher. These results are consistent with earlier findings for discharges with forward versus reversed magnetic field and fixed X-point location [63, 64] and point to a puzzle not explained satisfactorily by present theoretical models: threshold studies consistently show a transition condition related to edge electron temperature, but it is topology dependent. The central toroidal velocity is also seen to ramp towards the co-current direction in

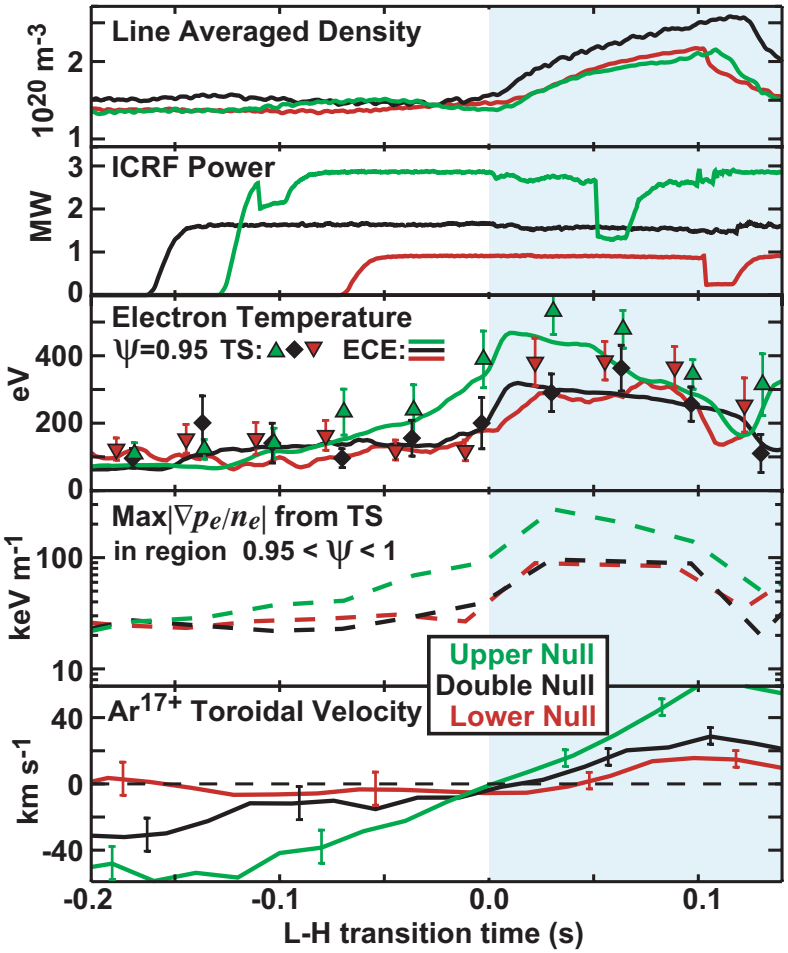


**Figure 19.** Time traces from LSN, DN and USN discharges ($B \times \nabla B$ down) with nearly identical $I_p$, $B_T$ and $\bar{n}_e$. ICRF power is applied to induce an L–H transition. The time axis is offset, placing zero near the time of transition. Edge electron temperatures are measured by electron cyclotron emission (ECE) and edge Thomson scattering (TS). Electron pressure gradients at the 95% flux surface are shown as dashed lines. The time of L–H transition is seen to coincide with central toroidal rotation (measured via $Ar^{17+}$ Doppler) achieving roughly the same value ($\sim$0 km s$^{-1}$ in this case), independent of magnetic topology. In contrast, USN edge electron temperatures and pressure gradients are clearly different from LSN.

response to increased auxiliary power (discussed further below). Remarkably, at the time of L–H transition, the velocity achieves a level near $\sim$0 km s$^{-1}$, independent of magnetic topology!

A comparison of toroidal velocities measured at the plasma centre and 2 mm outside the separatrix is shown in figure 20. These discharges are similar to those of figure 19 but had different ICRF power levels. Unfortunately, owing to the high power densities, the probes were restricted to $\rho \geqslant 2$ mm and could not be operated at all in the highest power discharges. Nevertheless, the correspondence between central and near-separatrix velocities in these ICRF-heated L-mode phases is similar to that in Ohmic L-mode plasmas (such as in figure 18(*b*), with a proportionality of roughly $\sim$1.5). Apparently, the central velocity simply follows changes in plasma rotation near the separatrix (perhaps with a time-delay, as seen during the L–H transition [23]). In effect, the central rotation is a crude measure of the separatrix plasma rotation during the L-mode phase and, by inference, relates to the radial electric field there (allowing for offsets that may include rotation profile effects).

These data suggest that at least two elements can control plasma rotation near the separatrix, both of which appear to influence the L–H transition physics in a somewhat additive fashion for these discharges: the SOL flow boundary conditions, which change in going from LSN to USN, and a co-current flow drive mechanism, perhaps related to the edge plasma pressure gradients that are affected by the input power. We do not offer an explanation for the latter response here. However, a similar effect has been observed during the H-mode phase of Ohmic or ICRF heated plasmas [25]; the level of central plasma rotation was found to correlate with plasma stored energy. A number of explanations have been advanced for this behaviour, including theories based on plasma turbulence [65, 66] and sub-neoclassical transport [67].

Finally, it is important to note that during the H-mode phase, the correspondence between probe-inferred separatrix plasma rotation and central plasma rotation is lost; the central plasma can co-rotate at speeds up to 120 km s$^{-1}$. These observations indicate that the toroidal rotation profile inside the separatrix changes dramatically during the H-mode. Thus, while SOL flow boundary conditions appear to affect the L–H

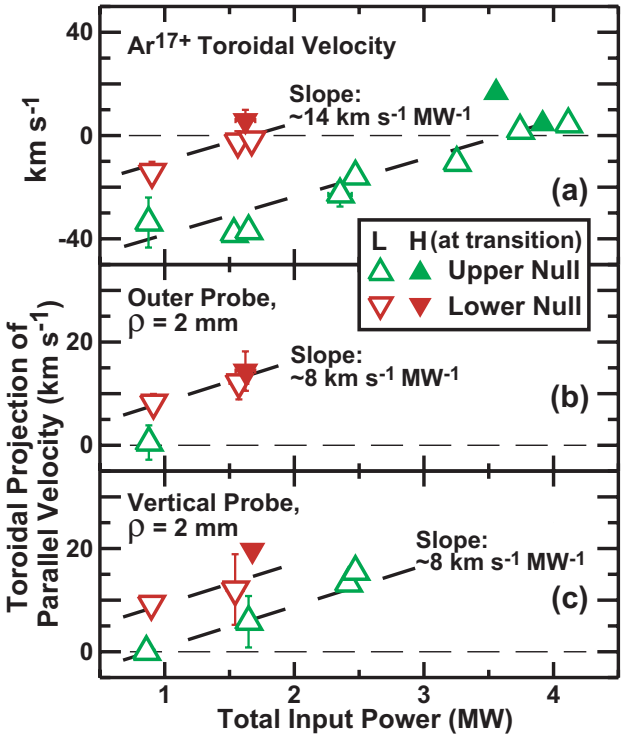


**Figure 20.** Toroidal velocities at the plasma centre and 2 mm into the SOL as a function of total input power in otherwise identical plasmas (Ohmic power level corresponds to leftmost data points). Magnetic topology and input power combine to affect central and edge toroidal velocities. The L–H transition is seen when central rotation achieves roughly the same value in these discharges.

transition, they do not appear to play a dominant role in setting the rotation of the core plasma once the H-mode is achieved.

## 7. Summary and conclusions

Detailed measurements of plasma profiles, including flows, in the low-field (inner) and high-field (outer) side SOL regions of Alcator C-Mod have been performed in discharges with different magnetic separatrix topologies (upper-, lower- and double-null) and with a range of plasma densities. From a variety of measures, these data reveal a strong poloidal asymmetry (ballooning-like) in cross-field transport: $T_e$ gradients along field lines, in/out variation in fluctuation levels (persistent in single-null) and in/out pressure asymmetries (particularly evident in double-null). Dramatic, near-sonic parallel plasma flows are detected in the high-field SOL. These flows tend to reverse sign in changing from upper to lower X-point location and are robustly insensitive to discharge density for the factor of ∼2 variation studied. The drive mechanism is clearly connected to a ballooning-like transport asymmetry, hence their designation as *transport-driven flows*. In contrast, parallel flows on the outer SOL are not as strong (factor of ∼3 smaller) and modulate with X-point changes, but tend to remain in the co-current direction. They also exhibit a clear sensitivity to discharge density. This behaviour, plus separate information on poloidal velocities, suggests that these flows are more closely associated with toroidal plasma rotation and Pfirsch–Schlüter ion currents.

A simple magnetic flux-tube model is used to explore the transport-driven component of the flows. Measurements indicate that the thermal plus flow energy density is roughly constant along a flux tube. However, the reduction in flux-tube cross-section in the high-field region can lead to a 'nozzle effect', accelerating the local plasma flow. A match between measured and modelled flow velocities can be achieved by postulating a very strong ballooning-like asymmetry to the cross-field transport. The implied cross-field convection and diffusion coefficients are found to be similar in magnitude to those from previous analyses, including the trends of increasing transport with distance from the separatrix and discharge density. The model also clearly demonstrates that transport-driven flows can lead to a net volume-averaged toroidal momentum in the SOL, co-current directed when $B \times \nabla B$ is pointing towards the X-point, counter-current directed otherwise.

With regard to impurity transport in the SOL, the overall plasma convection pattern would appear to promote the migration of impurities born from main-chamber plasma–wall contact towards the inner divertor strike point (particularly from high-field side wall surfaces, as demonstrated directly from impurity plume dispersal experiments). However, the flow pattern does not appear to allow impurities to be swept directly from the outer to the inner divertor; the net poloidal flow is found to be stagnant near the outer midplane. Such a flow field is broadly consistent with one that has been speculated to exist in JET to explain the buildup of carbon in the inner divertor [68] and to account for plasma flow observations at the top of the vessel [9]. The flow field is also consistent with recent measurements of $^{13}$C deposition following $^{13}CH_4$ injection in JET [69]: $^{13}CH_4$ injected at the top of the vessel resulted in $^{13}$C deposition on the inner divertor tiles.

A comparison of toroidal plasma flow velocities measured near the separatrix (via probes) with that in the plasma centre (via $Ar^{17+}$ Doppler) shows the two to be closely connected; in changing from upper- to lower-null with $B \times \nabla B$ pointing down, both exhibit an incremental change towards the co-current direction. The change in central plasma rotation is found to be nearly proportional to that measured at the separatrix in the low-field side SOL. These data clearly indicate that SOL flows can impose influential boundary conditions on the confined plasma. Moreover, transport-driven flows appear to affect toroidal rotation in the SOL itself; a stronger (weaker) radial electric field is evident when $B \times \nabla B$ is pointing towards (away from) the X-point. These observations are particularly intriguing since they suggest a broader connection to L–H threshold physics: radial electric field gradients (velocity shear) at the edge are thought to play a key role, while magnetic topology is known empirically to affect L–H power thresholds.

Results from a set of matched ICRF-heated discharges are presented, exploring the behaviour of central plasma rotation and SOL flows as the L–H transition is approached in upper-, lower- and double-null topologies. Remarkably, the L–H transition is found to be coincident with central rotation, achieving roughly the same value in these discharges, independent of topology. Since transport-driven SOL flows tend to impede co-current rotation in upper-null, a higher input power (which tends to spin the plasma in the co-current direction) is correspondingly required. We recognize that the

physics controlling the L–H transition is expected to involve plasma flow gradients (i.e. $E \times B$ shear zones) that are not directly measured in these experiments. Nevertheless, these results clearly link the boundary conditions imposed by SOL flows to the empirically observed topology dependence of the L–H power threshold.

## Acknowledgments

We thank Ben Carreras for his constructive comments on this paper. The data presented in this paper would not have been collected without the continuing dedication and hard work of the engineers, technical staff, students and scientists on the Alcator team. This work is supported by US DoE Coop. Agreement DE-FC02-99ER54512.

## References

[1] Wan A.S., LaBombard B., Lipschultz B. and Yang T.F. 1987 *J. Nucl. Mater.* **145–147** 191
[2] Vershkov V.A., Grashin S.A. and Chankin A.V. 1987 *J. Nucl. Mater.* **145** 611
[3] Vershkov V.A. 1989 *J. Nucl. Mater.* **162** 195
[4] Pitts R.A., Vayakis G., Matthews G.F. and Vershkov V.A. 1990 *J. Nucl. Mater.* **176** 893
[5] Boucher C., MacLatchy C.S., Le Clair G., Lachambre J.L. and St-Onge M. 1990 *J. Nucl. Mater.* **176** 1050
[6] MacLatchy C.S. *et al* 1992 *J. Nucl. Mater.* **196–198** 248
[7] LaBombard B. *et al* 1997 *J. Nucl. Mater.* **241–243** 149
[8] Asakura N. *et al* 1999 *Nucl. Fusion* **39** 1983
[9] Erents S.K., Chankin A.V., Matthews G.F. and Stangeby P.C. 2000 *Plasma Phys. Control. Fusion* **42** 905
[10] Asakura N. *et al* 2003 *J. Nucl. Mater.* **313–316** 820
[11] LaBombard B., Gangadhara S., Lipschultz B. and Pitcher C.S. 2003 *J. Nucl. Mater.* **313–316** 995
[12] Pitts R. 2004 private communication on flow measurements in TCV
[13] Philipps V., Roth J. and Loarte A. 2003 *Plasma Phys. Control. Fusion* **45** 17
[14] Hugill J. 1992 *J. Nucl. Mater.* **196** 918
[15] Chankin A.V. *et al* 2001 *J. Nucl. Mater.* **290** 518
[16] Chankin A.V. and Stangeby P.C. 2001 *Nucl. Fusion* **41** 421
[17] Porter G.D. *et al* 2003 *J. Nucl. Mater.* **313–316** 1085
[18] Rozhansky V. *et al* 2003 *J. Nucl. Mater.* **313–316** 1141
[19] Asakura N. *et al* 2000 *Phys. Rev. Lett.* **84** 3093
[20] Asakura N. *et al* 2004 *Nucl. Fusion* **44** 503
[21] LaBombard B. and Lipschultz B. 1987 *Nucl. Fusion* **27** 81
[22] Rozhansky V. and Tendler M. 1994 *Phys. Plasmas* **1** 2711
[23] Rice J.E. *et al* 2004 *Nucl. Fusion* **44** 379
[24] Lee W.D. *et al* 2003 *Phys. Rev. Lett.* **91** 205003
[25] Rice J.E. *et al* 2001 *Nucl. Fusion* **41** 277
[26] Smick N., LaBombard B. and Pitcher C.S. 2004 Plasma profiles and flows in the high-field side scrape-off-layer in Alcator C-Mod *J. Nucl. Mater.* submitted
[27] Hutchinson I.H. *et al* 1994 *Phys. Plasmas* **1** 1511
[28] Hutchinson I.H. 1988 *Phys. Rev.* A **37** 4358
[29] LaBombard B. *et al* 1999 *J. Nucl. Mater.* **266–269** 571
[30] Pitcher C.S. *et al* 2001 *Rev. Sci. Instrum.* **72** 103
[31] Matthews G.F. *et al* 1990 *Plasma Phys. Control. Fusion* **32** 1301
[32] Granetz R.S., Hutchinson I.H., Gerolamo J., Pina W. and Tsui C. 1990 *Rev. Sci. Instrum.* **61** 2967
[33] Lao L.L. *et al* 1985 *Nucl. Fusion* **25** 1611
[34] Rice J.E. *et al* 1998 *Nucl. Fusion* **38** 75
[35] Hutchinson I.H., Rice J.E., Granetz R.S. and Snipes J.A. 2000 *Phys. Rev. Lett.* **84** 3330
[36] Hutchinson I.H. 2002 *Principles of Plasma Diagnostics* (Cambridge, New York: Cambridge University Press)
[37] Terry J.L. *et al* 2003 *Phys. Plasmas* **10** 1739
[38] Boswell C.J., Terry J.L., LaBombard B., Lipschultz B. and Pitcher C.S. 2004 Plasma density profile of the inner scrape-off-layer of near double null discharges in the Alcator C-Mod tokamak *Plasma Phys. Control. Fusion* **46** 1247
[39] LaBombard B. *et al* 2001 *Phys. Plasmas* **8** 2107
[40] Gangadhara S. and LaBombard B. 2004 Impurity plume experiments in the edge plasma of the Alcator C-Mod tokamak *Plasma Phys. Control. Fusion* **46** 1617
[41] Jablonski D. *et al* 1997 *J. Nucl. Mater.* **241–243** 782
[42] Greenwald M. *et al* 1988 *Nucl. Fusion* **28** 2199
[43] Stangeby P.C. 1984 *Phys. Fluids* **27** 682
[44] Langley R.A., Bohdansky J., Eckstein W., Mioduszewski P., Roth J., Taglauer E., Thomas E.W., Verbeek H. and Wilson K.L. 1984 Data Compendium for Plasma–Surface Interactions *Nucl. Fusion, Special Issue 1984* (Vienna: IAEA)
[45] LaBombard B. 2002 *Phys. Plasmas* **9** 1300
[46] Wootton A.J. 1990 *J. Nucl. Mater.* **176** 77
[47] Meier M.A., Bengtson R.D., Hallock G.A. and Wootton A.J. 2001 *Phys. Rev. Lett.* **87** 085003
[48] Boedo J.A. *et al* 2001 *Phys. Plasmas* **8** 4826
[49] Braginskii S.I. 1965 Transport Processes in a Plasma *Reviews of Plasma Physics* (New York: Consultants Bureau) p 205
[50] Zawaideh E., Najmabadi F. and Conn R.W. 1986 *Phys. Fluids* **29** 463
[51] Hidalgo C. *et al* 2003 *Phys. Rev. Lett.* **91** 065001
[52] LaBombard B. *et al* 2000 *Nucl. Fusion* **40** 2041
[53] Umansky M.V., Krasheninnikov S.I., LaBombard B., Lipschultz B. and Terry J.L. 1999 *Phys. Plasmas* **6** 2791
[54] LaBombard B. *et al* 2003 *Fusion Energy 2002: Proc. 19th Int. Conf. (Lyon, 2002)* (Vienna: IAEA) CD ROM file EXD2_1 and http://www.iaea.org/programmes/ripc/physics/fec2002/html/fec2002.htm
[55] Biglari H., Diamond P.H. and Terry P.W. 1990 *Phys. Fluids* **2** 1
[56] Burrell K.H. 1997 *Phys. Plasmas* **4** 1499
[57] Terry P.W. 2000 *Rev. Mod. Phys.* **72** 109
[58] Connor J.W. and Wilson H.R. 2000 *Plasma Phys. Control. Fusion* **42** 1
[59] Groebner R.J., Burrell K.H. and Seraydarian R.P. 1990 *Phys. Rev. Lett.* **64** 3015
[60] Ryter F. and H Mode Database Working Group 1996 *Nucl. Fusion* **36** 1217
[61] Hughes J.W. *et al* 2001 *Rev. Sci. Instrum.* **72** 1107
[62] Carlstrom T.N. *et al* 1999 *Nucl. Fusion* **39** 1941
[63] Hubbard A.E. *et al* 1997 *Fusion Energy 1996: Proc. 16th Int. Conf. (Montreal, 1996)* (Vienna: IAEA) p 875
[64] Hubbard A.E. *et al* 1998 *Plasma Phys. Control. Fusion* **40** 689
[65] Shaing K.C. 2001 *Phys. Rev. Lett.* **86** 640
[66] Coppi B. 2002 *Nucl. Fusion* **42** 1
[67] Rogister A.L., Rice J.E., Nicolai A., Ince-Cushman A. and Gangadhara S. 2002 *Nucl. Fusion* **42** 1144
[68] Coad J.P. *et al* 2001 *J. Nucl. Mater.* **290–293** 224
[69] Likonen J. *et al* 2003 *Fusion Eng. Design* **66–68** 219